



**HAL**  
open science

## Subsurface connections in the eastern tropical Pacific during La Niña 1999-2001 and El Niño 2002-2003

Ivonne Montes, Wolfgang Schneider, François Colas, Bruno Blanke, Vincent Echevin

► **To cite this version:**

Ivonne Montes, Wolfgang Schneider, François Colas, Bruno Blanke, Vincent Echevin. Subsurface connections in the eastern tropical Pacific during La Niña 1999-2001 and El Niño 2002-2003. *Journal of Geophysical Research. Oceans*, 2011, 116, pp.C12022. 10.1029/2011JC007624 . hal-00743473

**HAL Id: hal-00743473**

**<https://hal.science/hal-00743473>**

Submitted on 4 Jan 2022

**HAL** is a multi-disciplinary open access archive for the deposit and dissemination of scientific research documents, whether they are published or not. The documents may come from teaching and research institutions in France or abroad, or from public or private research centers.

L'archive ouverte pluridisciplinaire **HAL**, est destinée au dépôt et à la diffusion de documents scientifiques de niveau recherche, publiés ou non, émanant des établissements d'enseignement et de recherche français ou étrangers, des laboratoires publics ou privés.

Copyright

## Subsurface connections in the eastern tropical Pacific during La Niña 1999–2001 and El Niño 2002–2003

Ivonne Montes,<sup>1,2</sup> Wolfgang Schneider,<sup>2,3</sup> Francois Colas,<sup>4,5</sup> Bruno Blanke,<sup>6</sup> and Vincent Echevin<sup>5</sup>

Received 23 September 2011; revised 11 October 2011; accepted 11 October 2011; published 16 December 2011.

[1] The subsurface connections between the Equatorial Current System (ECS) and the Peru Current System (PCS) between 1999 and 2005 are investigated with a primitive-equation, eddy-resolving regional model that is forced with realistic atmospheric and lateral oceanic conditions. Specific attention is given to the 1999–2000 La Niña and the 2002–2003 El Niño. The model's skill is assessed through a comparison with satellite-derived sea level anomalies and in situ sea surface temperature time series. The model reproduces fairly well the known dynamics of the region for climatological conditions, and the numerical solution obtained for the particular 1999–2000 and 2002–2003 events presents patterns rather typical of cold and warm phases of El Niño–Southern Oscillation (ENSO). Eulerian and Lagrangian diagnoses are used to derive relevant information about the density and velocity vertical structures of the ECS and the PCS. The transports of the major currents in the region are shown to differ a lot between the 1999–2000 La Niña and the 2002–2003 El Niño. The equatorial subsurface currents transfer significantly more water into the eastern tropical Pacific during La Niña than during El Niño, whereas the Peru–Chile Undercurrent (PCUC) carries more water during El Niño. The equatorial subsurface currents, and especially the primary Southern Subsurface Countercurrent, contribute to 80% of the PCUC transport during the 1999–2000 cold phase. This ratio falls down to only 20% during the 2002–2003 warm phase.

**Citation:** Montes, I., W. Schneider, F. Colas, B. Blanke, and V. Echevin (2011), Subsurface connections in the eastern tropical Pacific during La Niña 1999–2001 and El Niño 2002–2003, *J. Geophys. Res.*, 116, C12022, doi:10.1029/2011JC007624.

### 1. Introduction

[2] The El Niño–Southern Oscillation (ENSO) has been widely studied, especially because of its impact on marine biological productivity and the climate of the Americas [Wang and Fiedler, 2006]. This phenomenon is characterized by an irregular interannual oscillation of tropical Pacific upper ocean temperatures and is the strongest climate variation on time scales ranging from a few months to several years [Wang and Picaut, 2004; Latif and Keenlyside, 2009].

[3] Under normal conditions, the trade winds accumulate warm surface water in the western Pacific and draw colder

upwelled water to the surface along the equator in the eastern Pacific. Hence, the zonal sea surface temperature (SST) gradient is eastward and the thermocline is pushed down in the west and elevated in the east [McPhaden, 2004; McPhaden et al., 2006]. Variations in the strength of the trade winds generate equatorially trapped baroclinic disturbances at several time scales in the western Pacific. These disturbances propagate eastward in the shape of equatorial Kelvin waves and are held responsible for the transmission of equatorial variability all the way to the South American coast; they propagate eventually poleward as coastal-trapped waves [Enfield and Allen, 1980; Brainard and McLain, 1987]. At the interannual scale, changes in these winds can break down or reinforce the east–west surface temperature contrast and shoal or deepen the equatorial thermocline, altering the propagation of equatorial waves. Furthermore, the variability of the trade winds modifies the circulation patterns at the ocean surface and subsurface [Fiedler et al., 1992; Strub et al., 1998; Blanco et al., 2002; Wang and Fiedler, 2006; Colas et al., 2008]. A remarkable effect is the weakening or even disappearance of the Equatorial Undercurrent (EUC) during the ENSO warm phases (El Niño events), in contrast to its strengthening during the cold phases (La Niña events) [McPhaden and Hayes, 1990; Kessler and McPhaden, 1995; Izumo et al., 2002].

<sup>1</sup>Programa de Postgrado en Oceanografía, Departamento de Oceanografía, Universidad de Concepción, Concepción, Chile.

<sup>2</sup>Centro de Investigación Oceanográfica en el Pacífico Sur-Oriental (Fondap-Copas), Universidad de Concepción, Concepción, Chile.

<sup>3</sup>Departamento de Oceanografía, Universidad de Concepción, Concepción, Chile.

<sup>4</sup>Institute of Geophysics and Planetary Physics, University of California, Los Angeles, California, USA.

<sup>5</sup>Laboratoire d'Océanographie et du Climat Expérimentation et Approches Numériques, IRD/IPSL/UPMC, Paris, France.

<sup>6</sup>Laboratoire de Physique des Océans, UMR 6523, CNRS/Ifremer/IRD/UBO, Brest, France.

[4] The EUC is one major component of the Equatorial Current System (ECS) that lies beside and in connection with the Peru Current System (PCS). The feeding of the Peru-Chile Undercurrent (PCUC) by the eastward subsurface equatorial currents (EUC and the primary and Southern Subsurface Countercurrent (pSSCC) and secondary Southern Subsurface Countercurrent (sSSCC)) under normal atmospheric and oceanic conditions shows evidence of the ECS-PCS interaction [Lukas, 1986; Johnson and Moore, 1997; McCreary et al., 2002; Montes et al., 2010]. The PCUC is part of the PCS, flows poleward over the shelf slope, and is an important source of productive coastal upwelled waters off Peru owing to its high nutrient content [e.g., Huyer et al., 1987].

[5] Considering how direct and important the connection between these two current systems is, the PCS ought to be strongly affected by the ENSO variability, with occurrence of interannual variability in currents such as the PCUC. Furthermore, sustained advection of warm waters from the ECS toward the Peruvian coast during El Niño events could have dramatic consequences on the regional climate. For example, the accumulation of anomalously warm water off Peru can generate an onshore geostrophic flow that can further delay the coastal upwelling recovery during El Niño [Colas et al., 2008].

[6] Therefore, our main interest here is to investigate how this connection is modified during the cold and warm phases of ENSO. We use a high-resolution numerical model to simulate the ocean circulation in the eastern tropical Pacific (ETP) for the period 1999–2005, and we address the following issues: (1) the impact of ENSO on the subsurface Equatorial Current System and the PCUC in the ETP, (2) the connections between the subsurface Equatorial Current System and the PCUC during contrasted ENSO conditions and (3) the transports associated with these different connections. According to the Niño3.4 index ([http://www.cpc.ncep.noaa.gov/products/analysis\\_monitoring/ensostuff/ensoyears.shtml](http://www.cpc.ncep.noaa.gov/products/analysis_monitoring/ensostuff/ensoyears.shtml)), our simulation period spans a strong La Niña (August 1999–July 2000), a moderate El Niño (May 2002–February 2003), and a weak El Niño (June 2004–February 2005). Our analysis focuses on the strong cold phase and the moderate warm phase.

[7] This paper is structured as follows. The description of the model and its validation are given in section 2. Section 3 provides the Eulerian description of the subsurface ECS and of the PCS and uses a Lagrangian analysis to understand their connections under contrasted ENSO conditions. Our conclusions are presented in section 4.

## 2. Methodology

### 2.1. Regional Ocean Model

[8] The numerical model employed in this work is the Regional Ocean Modeling System (ROMS). ROMS is a split-explicit, free-surface, primitive-equations ocean model, based on the Boussinesq approximation and hydrostatic vertical momentum balance. A complete description of ROMS is given by *Shechepetkin and McWilliams* [2005, 2009].

[9] The model domain covers the ETP from 22°S to 4°N and from 94°W to the South American coast (Figure 1). The spatial resolution is 1/9° (1–12 km) with 32 terrain-following vertical levels (with a higher resolution in the upper

ocean layer). The bottom topography is derived from the ETOPO2 (2' resolution) data set [*Smith and Sandwell*, 1997]. The model is run from August 1999 to December 2005, driven by wind stress derived from daily QuikSCAT satellite scatterometer data gridded at 1/2° resolution [*Liu et al.*, 1998]. The model is also forced by fresh water and heat fluxes extracted from the Comprehensive Ocean–atmosphere Data Set (COADS) ocean surface monthly climatology at 1/2° resolution [*Da Silva et al.*, 1994]. This data set is also used to restore model SST and sea surface salinity to climatological values through a heat–flux correction [*Barnier et al.*, 1995]. Five-day varying variables from the Simple Ocean Data Assimilation Parallel Ocean Program (SODA-POP) reanalysis version 2.4.3 [*Carton and Giese*, 2008] at 1/2° resolution are used to force our model at its three open boundaries (north, west, and south). Thus, the interannual signals related to ENSO variability are introduced in the model through its lateral boundaries as a remote oceanic forcing and through the regional wind stress as a local forcing. The SODA representation of August 1999 is also used as initial conditions. The model solution is considered stable after a 3 year spin-up that used the three-times-repeated first year (August 1999–July 2000) of the model forcing. Model outputs are averaged and stored on a daily basis. Preprocessing and postprocessing of the simulation were achieved partially with the use of ROMSTOOLS (<http://roms.mpl.ird.fr/>) [*Penven et al.*, 2008].

### 2.2. Lagrangian Algorithm

[10] The Lagrangian diagnoses are based on the off-line mass-preserving algorithm ARIANE (<http://www.univ-brest.fr/lpo/ariane/>) [*Blanke and Raynaud*, 1997; *Blanke et al.*, 1999], which is used here to calculate trajectories of numerical floats (particles) within the daily archive of our interannual, three-dimensional velocity field. The approach allows the full description of individual trajectories as well as volume transport estimates on the basis of the infinitesimal transport weight allotted to each numerical float and transported without alteration along its trajectory. The volume of water transported from an initial to a final geographical section is computed by simply summing the infinitesimal transport of the numerical floats that achieve the connection that is being considered.

[11] For this particular study, we run our Lagrangian diagnoses within the area that spreads from 10°S to 2.5°N and from 92°W to the west coast of South America. The edges of this domain are subdivided into five adjacent sections (Figure 1). The western section is set at 92°W, just west of the Galapagos Island. It strategically intercepts the equatorial currents relevant for our study and is used to define the release positions of all the numerical floats. The four other sections bound the domain north and south and correspond to possible contrasted destinations for the particles. The northern edge is located at 2.5°N and bears a northwestern section and a northeastern section that are delimited by longitudes 92°W and 83°W and by longitude 83°W and the coast of Colombia, respectively. The southern edge is located at 10°S and also bears two sections, a southwestern section and a southeastern section, that are delimited by longitudes 92°W and 82°W and by longitude 82°W and the Peruvian coastline, respectively.

[12] We focus on the connection achieved from the western section to the southeastern section since it corresponds to the

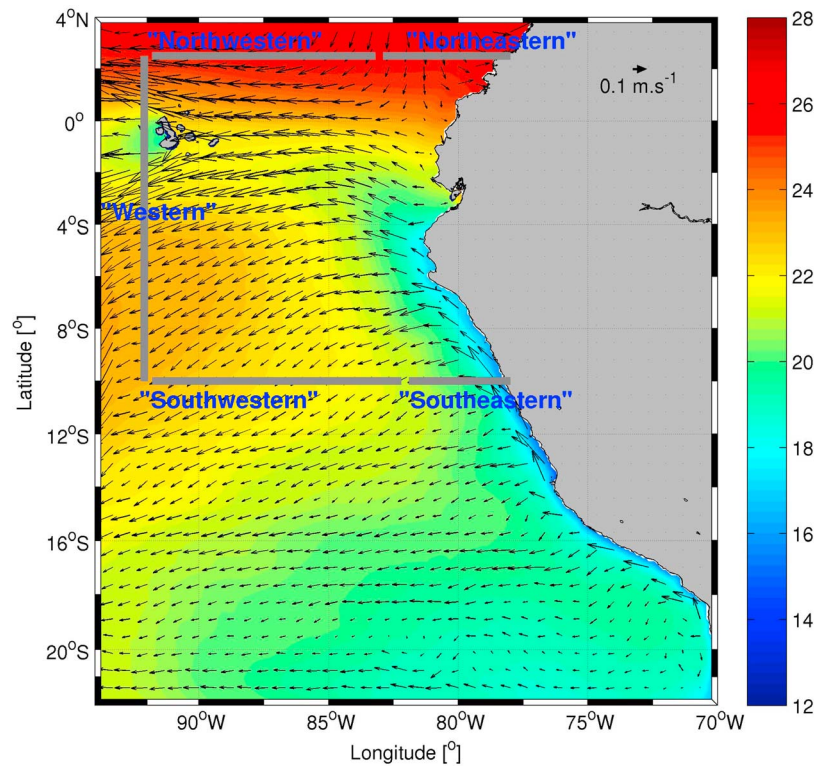


**Figure 1.** Model domain, mean surface currents (with one vector every fifth grid point), and SST (color shaded) of the interannual simulation. Current speed is scaled according to the reference vector located in the upper right hand corner. The color bar indicates temperature in °C. The area wherein Lagrangian experiments are carried out is bounded by gray solid lines and by the coast of South America, and the names of the corresponding five control sections are given in blue.

pathway of particles that travel from the ECS to the nearshore area occupied by the PCUC at 10°S (see section 3 for more details). To do this, millions of particles are initialized on the western section at depths above 400 m and in areas where the eastward zonal velocity exceeds  $0.01 \text{ m s}^{-1}$ , with the distribution in time and space proposed by *Blanke et al.* [1999] and with an individual weight, related to the local magnitude of the inflow, not to exceed in our case the maximum value of  $10^{-3} \text{ Sv d}^{-1}$  (with 1 Sverdrup =  $10^6 \text{ m}^3 \text{ s}^{-1}$ ). All particles are integrated forward in time until they reach one of the five previously defined control sections (see section 3.4 for more details), with a maximum integration time of 1000 days (about 2.75 years) allowed for completing the connection (all the particles exited the control domain within this time interval). The starting dates on the initial section range sequentially from the first day of the model archive (1 August 1999) until 31 July 2002. Insofar as the ocean model was run until the end of December 2005, this sampling strategy does allow all the released particles to complete their integration within the archive available for the interannual simulation.

### 2.3. Validation

[13] To evaluate the realism of our ROMS simulation, we compare the model outputs with three observational data sources: the sea level anomaly (SLA) derived from the monthly satellite data produced by Segment Sol Multi-missions d'Altimétrie, d'Orbitographie et de Localisation Précise/Data Unification and Altimeter Combination System

(SSALTO/DUACS) [*Ducet et al.*, 2000], SST from the monthly Advanced Very High Resolution Radiometer (AVHRR) Pathfinder product (<http://www.nodc.noaa.gov/sog/pathfinder4km/>) gridded at 4 km resolution, and the monthly SST data from six coastal stations of the Instituto del Mar del Perú (IMARPE, <http://www.imarpe.pe>).

[14] Figure 2 shows the comparison of monthly SLA maps (with respect to the mean sea level over August 1999–December 2005) for our model solution and satellite altimetry for two typical La Niña and El Niño situations, in October 1999 and November 2002, respectively. In accordance with ENSO dynamics [*McPhaden*, 2004], negative anomalies of  $\sim 6 \text{ cm}$  appear in the equatorial region and along the coast at the peak of the La Niña event, whereas an opposite pattern, with maximum positive anomalies of  $\sim 10 \text{ cm}$ , is prominent at the peak of the El Niño event, for both the model solution and the observations. The model shows fair agreement with observations for large-scale patterns and amplitudes. The coastal waveguide is in particular well reproduced during warm ENSO conditions. Some differences are of course noticeable, e.g., larger model positive SLAs in the southern half of the domain and a farther southward extension of the equatorial Kelvin wave observed in the model during El Niño. Part of the discrepancy can be attributed to the difference in spatial resolution (the gridded satellite data are available at  $1/3^\circ$  resolution) and to the existence of a blind zone in altimetry coverage near the coast.

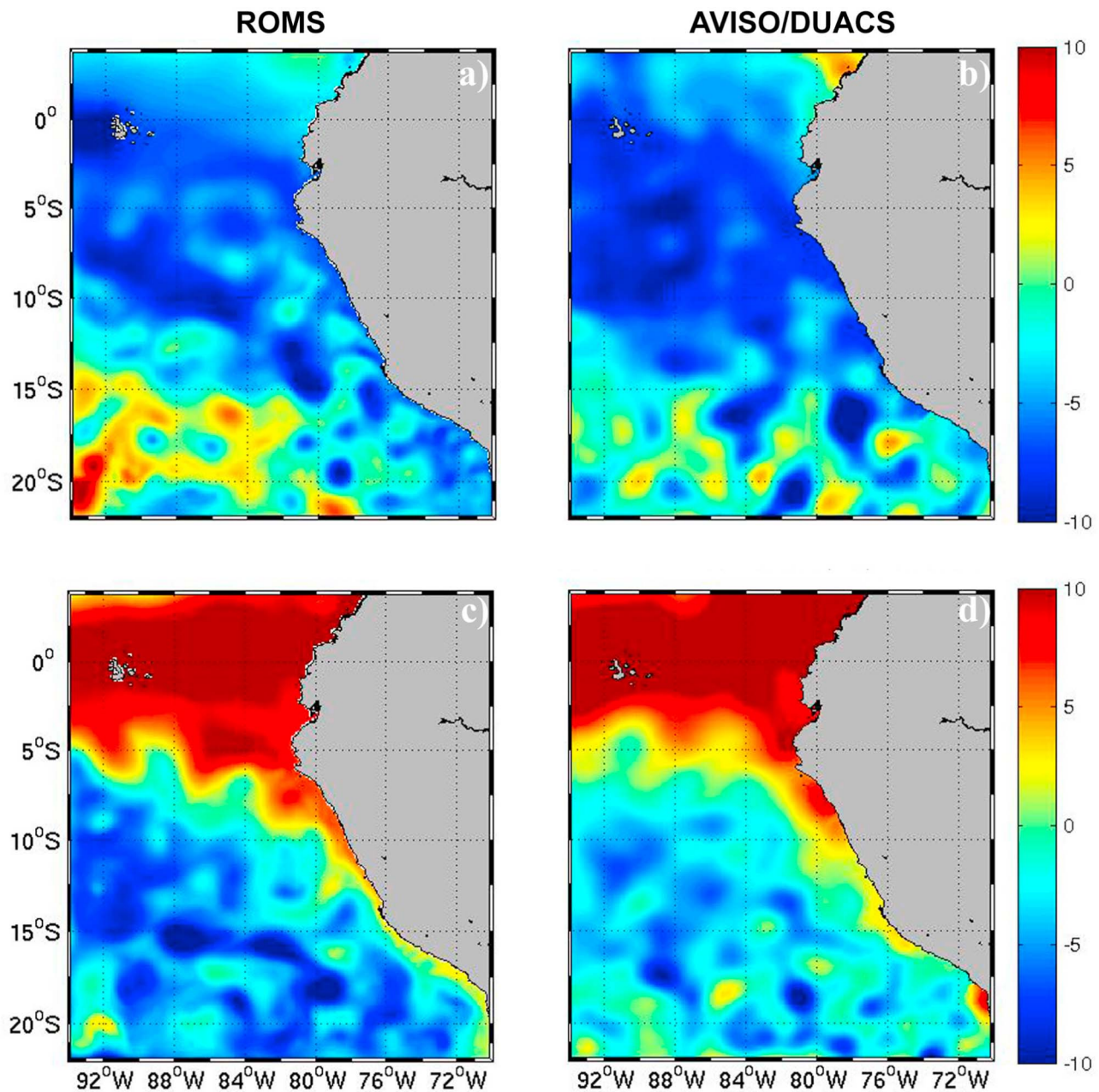


**Figure 2.** Monthly mean SLA maps from the model (Figures 2a and 2c) and AVISO/DUACS satellite altimetry (Figures 2b and 2d) during (a, b) the peak of La Niña (October 1999) and (c, d) El Niño (November 2002). The SLA is color shaded. The color bar indicates the SLA in cm.

[15] Figure 3 shows the model and AVHRR-Pathfinder SST for the two same characteristic months and emphasizes the major oceanographic patterns found during La Niña and El Niño events. During La Niña (Figures 3a and 3b), three main features characterize the regional dynamics: the cold upwelled water along the shore of Peru and northern Chile, the meridional SST gradient confined to the equator (mostly known as the equatorial front), and the cold tongue extending northwestward from the coast ( $\sim 5^{\circ}\text{S}$ ) to the equator. During El Niño (Figures 3c and 3d), the coastal upwelled water is about  $2^{\circ}\text{C}$  to  $3^{\circ}\text{C}$  warmer than during La Niña and is confined closer to the coast, the equatorial front is less pronounced and is shifted southward, and the cold tongue is replaced by

warmer water entering the eastern Pacific from the west. In general, the model reproduces fairly well these features, although it tends to overestimate the upwelling intensity near the coast, especially during La Niña. The wind product in use could explain this since the QuikSCAT data are known to overestimate the strength of the wind field within 50–100 km of the shoreline [Capet *et al.*, 2004; Croquette *et al.*, 2007; Colas *et al.*, 2011]. Over the whole domain, the model bias is of the order of  $-1^{\circ}\text{C}$  and  $-0.9^{\circ}\text{C}$  during the cold and warm events, respectively.

[16] Finally, we compare time series of model monthly SST anomalies (computed with respect to the average value over August 1999–December 2005) with equivalent data derived

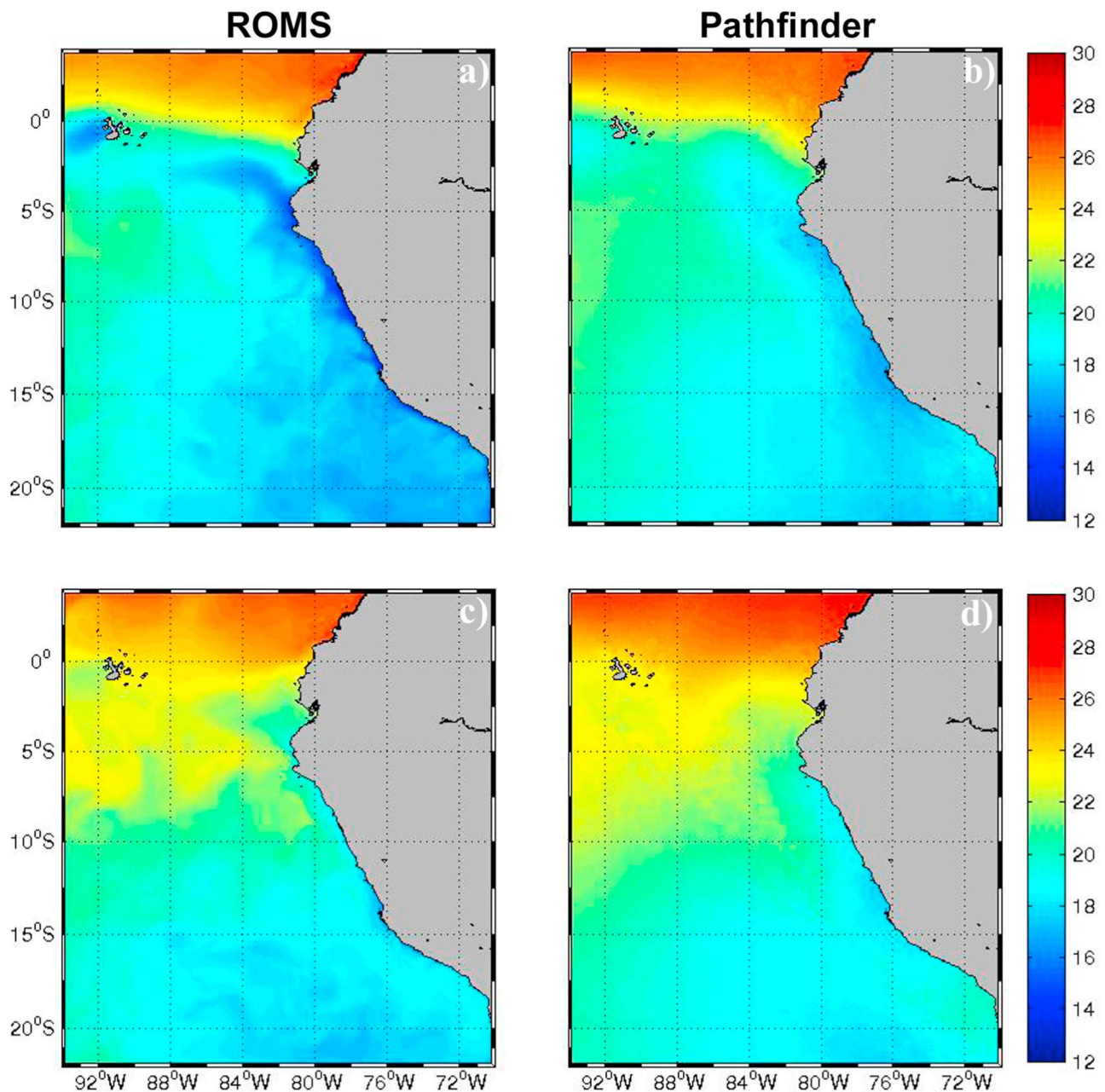


**Figure 3.** Monthly mean SST maps from the model (Figures 3a and 3c) and AVHRR-Pathfinder satellite (Figures 3b and 3d) data during (a, b) the peak of La Niña (October 1999) and (c, d) El Niño (November 2002). The SST is color shaded. The color bar indicates the SST in °C.

from IMARPE coastal stations located at Paita (5.06°S), Chiclayo (6.76°S), Chicama (7.72°S), Chimbote (9.05°S), Huacho (11.12°S), and Callao (12.06°S) (Figure 4). Some discrepancies are obvious, such as peaks underestimated by the model (e.g., in March 2002 for Paita, Chimbote, and Huacho). They can be attributed to the model spatial resolution, which is too coarse to resolve finely the nearshore processes, and to overestimation of the atmospheric forcing near the coast, which leads to colder than observed SSTs. Nevertheless, the comparison shows fair agreement between model and observed time series with a high linear correlation coefficient (0.74 to 0.87) except at the southernmost station

(0.58). Model and in situ data show both a pronounced seasonal signal, in phase, with peak values in summer.

[17] Furthermore, the mean state of our interannual numerical solution can be compared with the mean state of former ROMS climatological configurations obtained for about the same study area. Our solution closely matches that of *Penven et al.* [2005] as well as that of *Montes et al.* [2010] (e.g., SST bias of the order of 0.5°C and 0.3°C, respectively). Both above mentioned studies were forced with QuikSCAT-derived wind fields, but open boundary conditions were obtained from the Ocean Circulation and Climate Advanced Modeling (OCCAM) project [*Webb et al.*, 1997] and SODA model, respectively.

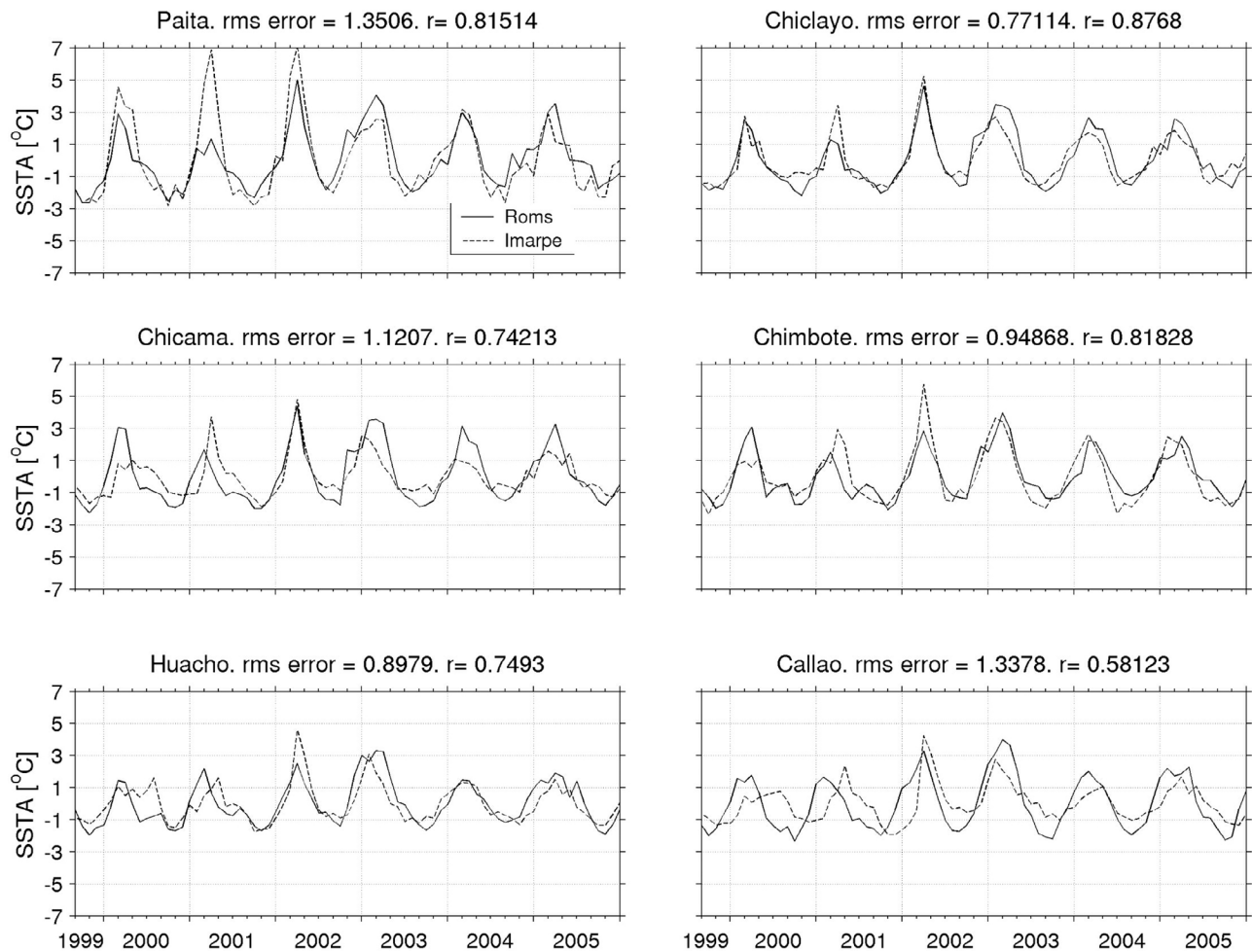


**Figure 4.** SSTA anomaly ( $^{\circ}\text{C}$ ) time series obtained from the model (solid line) and IMARPE data (dashed line) at six locations along the coast of Peru: Paitya ( $5.06^{\circ}\text{S}$ ), Chiclayo ( $6.76^{\circ}\text{S}$ ), Chicama ( $7.72^{\circ}\text{S}$ ), Chimbote ( $9.05^{\circ}\text{S}$ ), Huacho ( $11.12^{\circ}\text{S}$ ), and Callao ( $12.06^{\circ}\text{S}$ ). Observations were available for the entire period of the model simulation (August 1999–December 2005).

### 3. Results and Discussion

#### 3.1. An Eulerian View of the Equatorial Current System: Mean Conditions, La Niña, and El Niño

[18] In this section, we focus on the vertical structure of the ECS, especially the subsurface zonal currents, during the cold and warm phases of ENSO. Daily model outputs for the most representative months of each event are averaged at  $92^{\circ}\text{W}$ , just west of the Galapagos Islands, over the meridional section that will be used below to release numerical particles. We choose the periods October–December 1999 and October–December 2002 for La Niña and El Niño periods, respectively. Additionally, we use the mean current data of the interannual run for the years 1999–2005 to calculate a reference state. In order to study the behavior of the currents to the east of the Galapagos Islands, we also analyze their vertical structure at  $87^{\circ}\text{W}$ .

##### 3.1.1. Mean Conditions

[19] The ECS is formed by four main currents (Figure 5): the westward South Equatorial Current (SEC) at the surface and the eastward EUC and Tsuchiya jets (pSSCC and sSSCC) at the subsurface [e.g., Kessler, 2006]. Vertical sections of

modeled zonal velocities at  $92^{\circ}\text{W}$  clearly reproduce these dynamical structures under mean conditions. Near the surface, these currents include the divided lobes of the SEC after passing the Galapagos Islands and flowing westward north and south of the equator in the upper 50 m, with maximum mean velocities of  $40\text{--}50\text{ cm s}^{-1}$  (Figure 5a). Eastward flowing currents include the subsurface EUC that extends from  $2^{\circ}\text{S}$  to  $2^{\circ}\text{N}$  and from  $\sim 30$  to  $\sim 300$  m depth with a maximum mean velocity greater than  $30\text{ cm s}^{-1}$  at  $0^{\circ}$ ,  $\sim 100$  m; the pSSCC with a maximum mean velocity core of  $\sim 14\text{ cm s}^{-1}$  at  $\sim 4^{\circ}\text{S}$ , 100 m; and the sSSCC with a maximum mean velocity core of  $\sim 3\text{ cm s}^{-1}$  at  $\sim 7^{\circ}\text{S}$ , 170 m. At  $87^{\circ}\text{W}$ , before approaching the Galapagos Islands (Figure 5d), the SEC extends over the full meridional extent of the model domain and takes up the upper 50 m, exhibiting a maximum velocity core of  $\sim 30\text{ cm s}^{-1}$  at  $0.5^{\circ}\text{S}$ . The three equatorial subsurface currents show a slight eastward reduction in their velocity cores as well as in their latitudinal and vertical extents. The EUC core keeps flowing along the equator at  $\sim 100$  m depth, at  $\sim 22\text{ cm s}^{-1}$ , i.e., a decline of  $\sim 40\%$  compared with that of the upstream section. The cores of the pSSCC and sSSCC have maximum velocities of  $\sim 11$  and

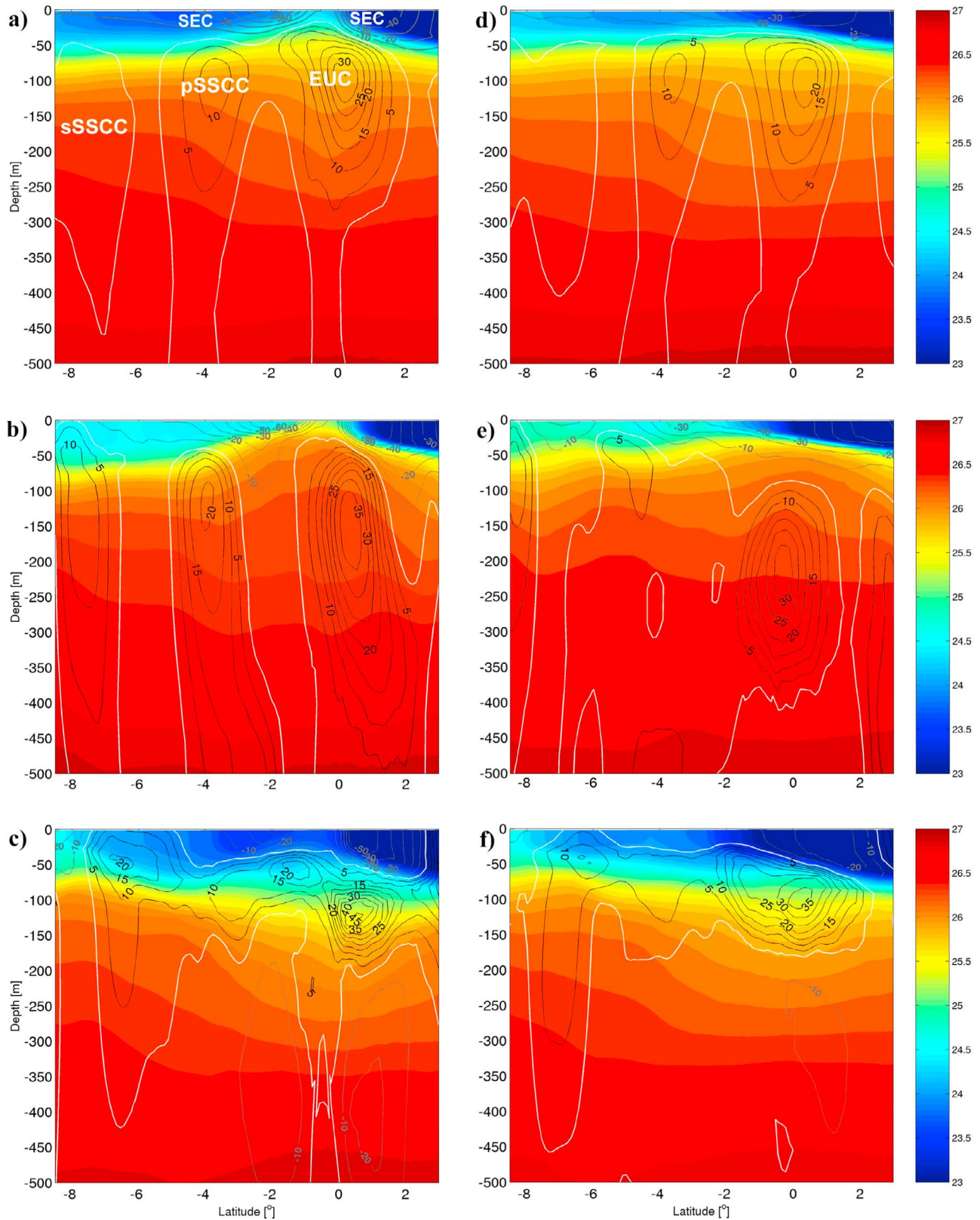


**Figure 5.** Vertical (0–500 m depth) sections of zonal velocity and density at 92°W (Figures 5a–5c) and 87°W (Figures 5d–5f) during (a, d) mean conditions (September 1999 – December 2005), (b, e) La Niña (September–December 1999), and (c, f) El Niño (September–December 2002) events. The density is color shaded, and the color bar indicates  $\sigma_t$  units. Solid black (gray) contours indicate eastward (positive) and westward (negative) flows, respectively. White contours mark zero velocity.

$\sim 2.5 \text{ cm s}^{-1}$ , respectively, showing a slight reduction inside the study region. Nevertheless, both currents keep their mean latitudinal and vertical positions at  $\sim 4^\circ\text{S}$ , 100 m, and  $\sim 7^\circ\text{S}$ , 170 m, respectively. Although the available observational data at  $92^\circ\text{W}$  are too scarce to allow a thorough comparison with our model outputs, this description with respect to depth, latitude, and associated velocities west of the Galapagos Islands is consistent with other model results [e.g., *Donohue et al.*, 2002] and observational data [e.g., *Johnson et al.*, 2002], as summarized by *Kessler* [2006]. This confirms the reasonable degree of realism of the model solution. Moreover, the vertical current structure of the ECS averaged between  $86^\circ\text{W}$  and  $87^\circ\text{W}$ , based on a climatological ROMS simulation and depicted by *Montes et al.* [2010, Figure 3] agrees with our interannual simulation despite different open boundary conditions and model domains. Insofar as our configuration includes the Galapagos Islands, our results confirm the reformation of the EUC after flowing around the archipelago, as proposed by *Steger et al.* [1998] and *Karnauskas et al.* [2007].

### 3.1.2. ENSO Cold Phase

[20] During the warm and cold phases of ENSO, the four currents are also present, but their features in depth and intensity along  $92^\circ\text{W}$  and  $87^\circ\text{W}$  are notably different from the mean conditions. During the 1999–2000 La Niña, at  $92^\circ\text{W}$  (Figure 5b), the SEC still reveals its two lobes, but the northern branch flows faster than the southern one ( $\sim 60 \text{ cm s}^{-1}$ ), with maximum mean velocities of  $\sim 70 \text{ cm s}^{-1}$ . The EUC is somewhat narrower ( $2^\circ\text{S}$ – $1^\circ\text{N}$ ) and exhibits a much deeper vertical extension (from  $\sim 30$  to 500 m depth), and its core is located deeper, near 150 m at the equator with a maximum velocity greater than  $35 \text{ cm s}^{-1}$ , i.e., a value close to mean conditions. The pSSCC also occupies a wider depth range (between  $\sim 50$  and  $>500$  m depth), and its core ( $3^\circ\text{S}$ – $4.6^\circ\text{S}$ ) is found slightly deeper at about 120 m near  $4^\circ\text{S}$  with maximum mean velocities  $\sim 22 \text{ cm s}^{-1}$ , thus stronger than under mean conditions. The core of the sSSCC ( $6.5^\circ\text{S}$ – $8^\circ\text{S}$ ) is centered somewhat shallower, close to 150 m at  $7.5^\circ\text{S}$ ; however, it has a stronger maximum mean velocity of  $\sim 13 \text{ cm s}^{-1}$ . In the same way as the other subsurface currents, the sSSCC exhibits its maximum vertical extension during La Niña conditions, with its upper boundary situated very close to the surface and extending down to around 500 m depth. The vertical structure of the currents at  $87^\circ\text{W}$  is much different (Figure 5e). Maximum velocities within the SEC still appear north of the equator, but also at the equator ( $\sim 20$ – $45 \text{ cm s}^{-1}$ ) where the SEC occupies the upper 100 m of the water column (instead of  $\sim 50$  m at  $92^\circ\text{W}$ , after flowing around of the Galapagos Islands). It spreads over the full meridional model domain, as under mean conditions. The EUC is slightly wider ( $2^\circ\text{S}$ – $1.5^\circ\text{N}$ ) than at  $92^\circ\text{W}$  and is confined to the subsurface between 100 and 400 m depth, with maximum core velocities of  $\sim 32 \text{ cm s}^{-1}$  at  $\sim 220$  m, which are significantly deeper than those close to the western boundary of the model domain. The pSSCC as such vanishes at  $87^\circ\text{W}$ ; only a small remnant subsists farther south ( $\sim 5^\circ\text{S}$ ) and much closer to the surface than west of the Galapagos Islands, with maximum velocities of  $\sim 7 \text{ cm s}^{-1}$ . The sSSCC is also situated farther south ( $\sim 8.5^\circ\text{S}$ ), with its upper limit at the surface and a maximum velocity core of  $\sim 11.5 \text{ cm s}^{-1}$ . Aside from the pSSCC at  $87^\circ\text{W}$ , all the subsurface currents are strengthened during the 1999 La Niña compared with mean conditions.

### 3.1.3. ENSO Warm Phase

[21] The vertical structure of the ECS during the 2002–2003 El Niño is also very distinct from mean conditions and contrasts with the structure found for the cold phase of ENSO. At  $92^\circ\text{W}$  (Figure 5c), the SEC maintains its typical two-lobe shape with its cores occupying the upper 70 m of the water column north ( $\sim 0.5^\circ\text{N}$ ) and south ( $\sim 1.5^\circ\text{S}$ ) of the equator, with velocities of 60 and  $30 \text{ cm s}^{-1}$ , respectively. The outcrop of the sSSCC between  $5^\circ$  and  $7^\circ\text{S}$  breaks its meridional continuity. At the subsurface, the most noticeable feature is the unification of the equatorial subsurface currents that appear mostly like one single current with three different cores. The EUC ( $1^\circ\text{S}$ – $2^\circ\text{N}$ ) has a drastically reduced vertical extension (from  $\sim 70$  to 200 m depth), its core shifts slightly northward and is located near 120 m depth, thus shallower than during La Niña, with a maximum mean velocity of  $45 \text{ cm s}^{-1}$ , which is stronger than during mean and La Niña conditions. The pSSCC shifts significantly northward ( $0.5^\circ\text{S}$ – $4^\circ\text{S}$ ) and is centered much shallower (close to 50 m depth at  $1^\circ\text{S}$ ) with mean maximum velocities of  $25 \text{ cm s}^{-1}$ , similar to La Niña conditions. It shows, however, a much less vertical extension (between 50 and  $\sim 120$  m) and a wider latitudinal extension than under mean and La Niña conditions. The core of the sSSCC is found at shallow depths of about 50 m, closer to the equator than during normal or cold conditions, around  $6.5^\circ\text{S}$ , with a maximum mean speed of  $20 \text{ cm s}^{-1}$ , i.e., the fastest configuration within all three scenarios. This current extends from 250 m depth to the surface and thus displays its minimal vertical extension of all three scenarios. Moreover, a westward current known as the Equatorial Intermediate Current (EIC) is visible during this period below the EUC. At  $87^\circ\text{W}$  (Figure 5f), the vertical structure of the ECS is basically the same as at  $92^\circ\text{W}$ , although the mean velocities and extensions of the currents are changed. The core of the SEC flows with maximum velocities smaller than  $25 \text{ cm s}^{-1}$  and is located slightly farther south than at  $92^\circ\text{W}$ . Again, its meridional extension is interrupted by the outcrop of the sSSCC, however, to a lesser extent. The EUC and the pSSCC cannot be distinguished from each other anymore. They flow between  $2.5^\circ\text{S}$  and  $2^\circ\text{N}$  and occupy the 50–150 m depth range as at the western section. The maximum mean core velocity is diminished from 45 to  $35 \text{ cm s}^{-1}$ . The core of the sSSCC is narrower than at  $92^\circ\text{W}$ ; its maximum velocity is found a bit shallower ( $\sim 30$  m depth) and slightly farther north, with a decreased maximum velocity of  $15 \text{ cm s}^{-1}$ . The EIC is also visible on this section between 200 and 500 m depth and with a maximum mean velocity of  $\sim 12 \text{ cm s}^{-1}$ . According to observational and numerical data, this current is permanently observed in the western and central tropical Pacific just under the EUC [*McPhaden*, 1984], but is visible in the ETP during El Niño events [*Rowe et al.*, 2000], as in our model solution.

[22] On the basis of observational data and numerical experiments, differences in the ECS between contrasted ENSO phases have already been reported. For example, *Izumo et al.* [2002] and *Izumo* [2005] noticed the relationship between EUC transport modulation on interannual time scales and zonal pressure gradients within the thermocline. They observed that the EUC was weak and even vanished for three months during the mature phase of the 1997–1998 El Niño while it was well established during La Niña after mid-1998. In our interannual solution, the EUC transport

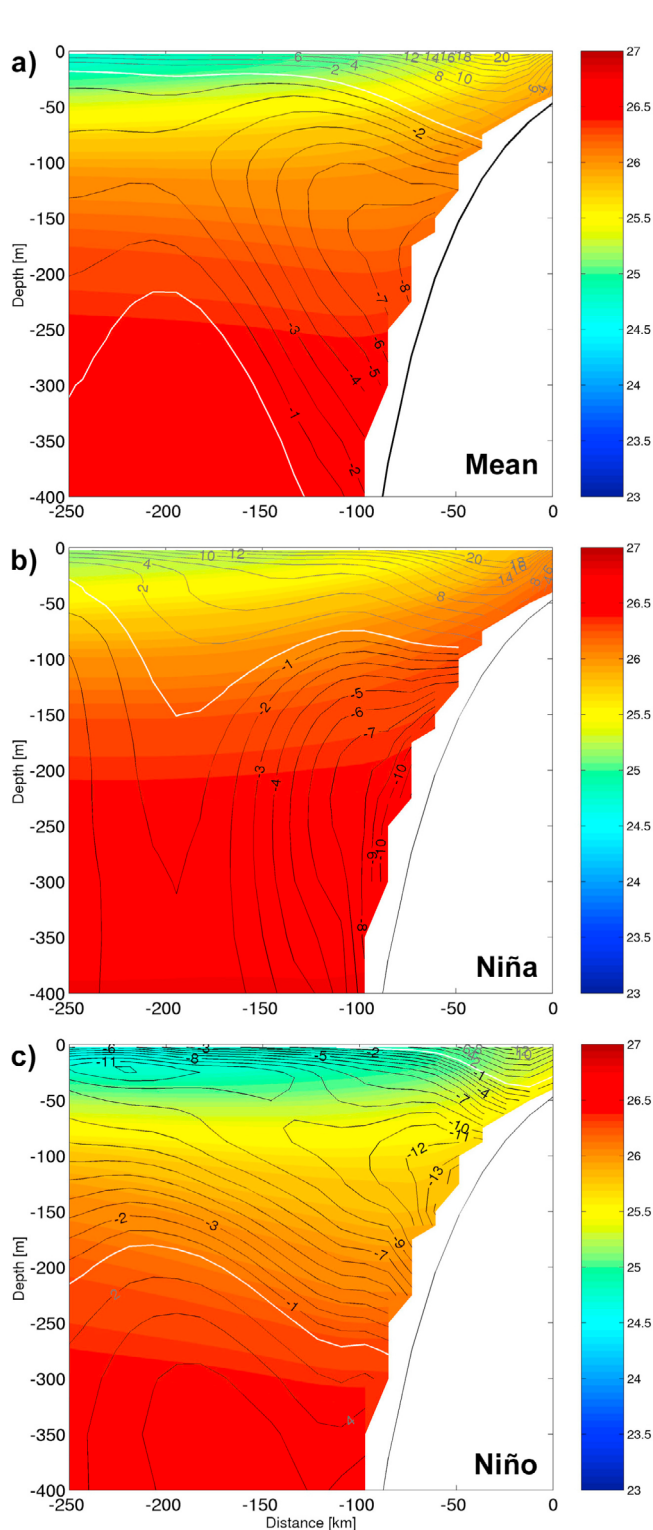


**Figure 6.** Vertical (0–400 m depth) sections of alongshore velocity and density averaged between 7°S and 13°S during (a) mean conditions (September 1999–December 2005), (b) La Niña (September–December 1999), and (c) El Niño (September–December 2002) events. The density is color shaded, and the color bar indicates  $\sigma_t$  units. Solid black (gray) contours indicate southward (negative) and northward (positive) flows, respectively. White contours mark zero velocity.

(defined here as the eastward flow greater than  $1 \text{ cm s}^{-1}$  in the latitude band 2°N to 2°S above 450 m depth) at 92°W shows a decrease of about 60% from the strong cold phase (Figure 5c) to the moderate warm phase (Figure 5b), with 17 and 8.4 Sv during La Niña and El Niño conditions, respectively; the EUC mean transport over 2000–2005 is  $\sim 10$  Sv. *Johnson et al.* [2002] explained this decrease in transport by the fact that the EUC is mainly driven by the trade winds, which build the zonal pressure gradient, that are weak during El Niño and strengthen during La Niña.

[23] On the other hand, little is known about the behavior of the Tsuchiya jets (pSSCC and sSSCC) during an ENSO event since most published studies address mean conditions. With an analytical model, *McCreary et al.* [2002] showed that the Tsuchiya jets could be geostrophic currents along fronts that are generated after a coastal or equatorial upwelling event, when Rossby wave characteristics converge or intersect in the interior ocean [see also *Colas et al.*, 2008]. We speculate here that any change on an interannual time scale (e.g., ENSO) could have an impact on this mechanism of generation and be responsible for variability of the jets. In our model solution, SSCCs transports are affected between the cold and warm phase; the pSSCC is substantially reduced by 50% (8.9 Sv, La Niña; 4.4 Sv, El Niño) while the sSSCC is reduced only by 10% (5.3 Sv, La Niña; 4.8, El Niño).

[24] Our results also show different signatures for the seawater density associated with these surface and subsurface flows. They are denser during La Niña and lighter during El Niño. This is consistent with the mechanisms responsible for ENSO: Stronger than normal trade winds during La Niña intensify the cold tongue that develops in the ETP owing to the relative shallowness of the thermocline that facilitates the upwelling of colder and denser than normal interior water. On the contrary, weaker trade winds allow the western Pacific warm pool to migrate eastward, reducing the area of the cold tongue during El Niño, warming the surface and pushing down the isopycnals [*McPhaden*, 2004], hence decreasing the density of the upper water column.

### 3.2. Eulerian View of the Peru Current System: Mean Conditions, La Niña, and El Niño

[25] In this section, we analyze the vertical structure of the PCS for average, La Niña, and El Niño conditions, focusing on its central portion between 7°S and 13°S (this area is known to be representative for the central Peru Current System since the bottom topography presents few alongshore variations [*Penven et al.*, 2005]), over which averages are computed. As in the previous section, we compute the mean of the most representative months for each event: October–December 1999 and October–December 2002 for La Niña and El Niño, respectively. The average is calculated from model current data integrated over the full interannual run (1999–2005). Figure 6 shows the alongshore velocity and density for the central PCS during the warm and cold phases of ENSO and for mean conditions. Noticeable changes in the current system as well as its stratification occur during La Niña and El Niño events.

[26] At the surface, under mean conditions, the Peru Coastal Current (PCC) flows nearshore equatorward, extending 250 km offshore over the first 50 m of the water column, with velocities up to  $20 \text{ cm s}^{-1}$ , close to shore but decreasing rapidly offshore, and amounts to about 0.5 Sv (Figure 6a)

(here and below the PCC transport is defined as the equatorward alongshore flow greater than  $1 \text{ cm s}^{-1}$ , extending up to 250 km offshore above 100 m depth). During La Niña conditions, the current spreads deeper ( $\sim 100 \text{ m}$ ), is slightly faster with mean maximum core velocities of about  $24 \text{ cm s}^{-1}$ , but still spreads over 250 km offshore (Figure 6b), likewise in mean conditions, and transports about 1.1 Sv. It is associated with slightly denser water than during normal conditions. During El Niño, the current is confined in a band not wider than 120 km, with a maximum velocity of only about  $12 \text{ cm s}^{-1}$ . It occupies only the first 40 m of the water column close to the coast while it shoals offshore (Figure 6c). It transports only  $\sim 0.1 \text{ Sv}$  and is associated with water slightly lighter than during normal conditions.

[27] The PCUC has been widely accepted as a major source for coastal upwelled waters [e.g., Huyer *et al.*, 1987]. Under mean conditions, it flows alongshore and poleward at subsurface levels over the continental slope, with its core located between 150 and 220 m. Its maximum mean speed is  $8 \text{ cm s}^{-1}$  near the slope, and it shows decreasing velocities toward the open ocean with an upward and westward tilt and an offshore extension of at least 250 km (Figure 6a). Its mean transport (defined here and below as the poleward alongshore flow  $> 1 \text{ cm s}^{-1}$  extending up to 250 km offshore above 400 m depth) is  $\sim 1.8 \text{ Sv}$ . Penven *et al.* [2005] provided evidence of a similar PCUC pattern on cross sections off Pisco ( $14^\circ\text{S}$ ), San Juan ( $15.7^\circ\text{S}$ ), and Arica ( $18.6^\circ\text{S}$ ) for climatological mean conditions and under the influence of a vigorous cyclonic wind stress curl (in agreement with Sverdrup dynamics). During La Niña (Figure 6b), the PCUC extends less offshore, only 150–200 km; its core is found deeper, between 200 and 300 m, with a mean maximum velocity of about  $11 \text{ cm s}^{-1}$  just off the continental shelf. It is thus slightly faster than during mean conditions. During El Niño (Figure 6c), the PCUC reaches an offshore extension over 250 km that is comparable to the mean conditions. Its vertical extension is heavily reduced since its upper limit is close to the surface, just below the PCC, and its lower limit is at  $\sim 250 \text{ m}$  at the level of the continental slope, bending upward offshore. Its velocity core is the fastest of all three scenarios and is around  $14 \text{ cm s}^{-1}$ , between 100 and 160 m, again attached to the continental slope (though an additional core is observed farther offshore, close to the surface). In this El Niño scenario, the PCUC spreads to at least 250 km offshore, which leads to a poleward transport of 3 Sv that is almost twice the value obtained for La Niña conditions (1.6 Sv) and mean conditions as well. As for the PCC, the PCUC is associated during La Niña (El Niño) with water slightly denser (lighter) than for normal conditions, in agreement with ENSO-related cold (warm) anomalies in the ETP upper ocean.

[28] To conclude, our interannual solution shows that during the warm period of ENSO the PCC is weakened while the PCUC is more intense (in speed as well as in transport) than under the other climatological conditions. This result is consistent with studies that showed that the PCUC reached velocities up to  $25 \text{ cm s}^{-1}$  during the strongest warm events, e.g., the 1997–1998 El Niño [Brink, 1982; Smith, 1983; Huyer *et al.*, 1991; Colas *et al.*, 2008].

[29] As already shown, disturbances of equatorial origin play an important role in modulating the PCUC at seasonal and interannual scales by triggering coastally trapped waves [e.g., Shaffer *et al.*, 1997; Pizarro *et al.*, 2002; Echevin *et al.*,

2011]. These poleward propagating waves modify the coastal currents particularly during ENSO [Colas *et al.*, 2008]. The increase in PCUC transport may seem at odds with the decrease of the equatorial subsurface currents during the warm phase. However, Montes *et al.* [2010] showed that under normal conditions the PCUC is only partly fed by equatorial currents. They found that  $\sim 30\%$  of the PCUC waters originate from the ECS through well-defined advective pathways and the other 70% from other sources. Thus, the PCUC is generated and forced by various factors (e.g., wind, alongshore pressure gradient). Consequently, variations in the ECS and PCUC transports do not necessarily correlate during normal conditions and ENSO events.

### 3.3. Typical Structures of the ECS and the PCS During El Niño and La Niña

[30] The previous descriptions of the ECS and the PCS are for one particular El Niño and La Niña period. One can legitimately wonder whether these structures are typical of general ENSO conditions off Peru, as important differences in large-scale anomalies during the onset of ENSO have been observed from one event to another [Wang and Fiedler, 2006]. Using the SODA reanalysis [Carton and Giese, 2008], for the period 1980–2000, composite velocity sections are constructed for El Niño and La Niña. Niño3.4 SODA SST indices greater than  $1^\circ\text{C}$  are used to define these periods (not shown). Over the years 1980–2000, we identify five El Niño and four La Niña events and obtain the vertical sections of a mean zonal velocity at  $92^\circ\text{W}$  and a mean alongshore velocity at  $12^\circ\text{S}$ , shown in Figure 7.

[31] The EUC core extends much deeper during La Niña than during El Niño mean conditions (Figures 7a and 7b), as for the 1999 and 2002 events (Figures 5b and 5c). Moreover, the modifications in the pSSCC structure between the cold and warm phases are rather similar for the composites and the 1999 and 2002 events. The sSSCC is barely visible in the composite sections, probably because of the coarser ( $0.5^\circ$ ) horizontal resolution used in SODA.

[32] For similar reasons, the PCUC is present in the composite analysis, but with a weaker intensity since it is less well resolved compared with ROMS. Nevertheless, it undergoes modifications during ENSO (Figures 7c and 7d) that are similar to the results of our regional model (Figures 6b and 6c). Its core is deeper and weaker during the cold phase ( $\sim 150\text{--}200 \text{ m}$ ;  $> 3 \text{ cm s}^{-1}$ ) than during the warm phase ( $100 \text{ m}$ ;  $7 \text{ cm s}^{-1}$ ).

[33] Even if ENSO events can differ from one event to the next, for instance because of contrasts in onset phase locking to the seasonal cycle and in local atmospheric conditions, we see strong similarities in the modifications of the ECS and the PCS during ENSO between the composite sections and the model simulation. This suggests that our numerical results are rather representative of typical ENSO conditions in the ETP, though they depend of course on the forcing used at the model open boundaries (here, SODA fields). The analysis of the differences that would stem from the use of other forcing fields is, however, beyond the scope of this study.

### 3.4. Fates of the Equatorial Subsurface Currents: EUC, pSSCC, and sSSCC

[34] In this section, by means of Eulerian and Lagrangian diagnoses, we investigate the circulation patterns in the ETP. We focus on the fates of the three equatorial subsurface

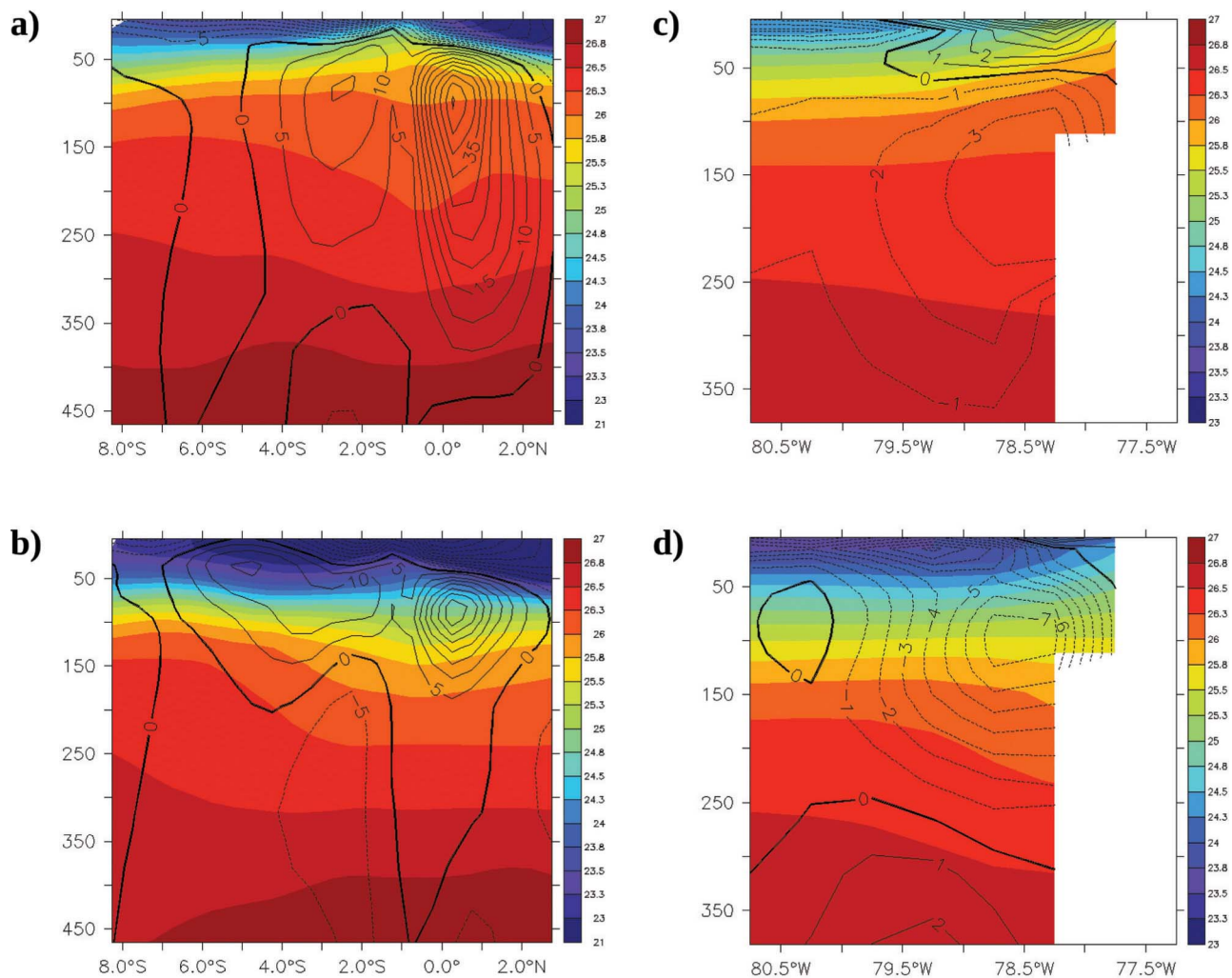


**Figure 7.** SODA composite vertical sections of zonal velocity and density at 92°W (Figures 7a and 7b) and alongshore velocity and density at 12°S (Figures 7c and 7d) during averaged (a, c) La Niña and (b, d) El Niño conditions. Composite sections are obtained from SODA outputs over the years 1980–2000. El Niño and La Niña periods are selected based on a Niño3.4 SODA SST index (see text for details). Solid (dashed) black contours indicate positive (negative) velocity. Thick solid black contours mark zero velocity.

currents (EUC, pSSCC and sSSCC) under mean conditions, and during the cold and warm phases of ENSO mostly by studying the contrasts obtained in EUC pathways.

### 3.4.1. EUC Pathways Diagnosed From Eulerian Mean Conditions

[35] Under mean conditions, the Galapagos Islands represent a topographic barrier to the EUC, causing it to split into two zonal branches, flowing north and south of the islands, that merge close to the equator just east of the archipelago [Steger *et al.*, 1998; Karinauskas *et al.*, 2007]. This feature is clearly confirmed by the mean horizontal Eulerian velocity field at 100 m depth of our high-resolution interannual simulation (Figure 8a). The strong EUC flow decreases by  $\sim 35\%$  ( $\sim 20\%$ ) in speed (transport) from 35 to 22  $\text{cm s}^{-1}$  (10 to 8 Sv) upon passing the Galapagos Archipelago. The remerged EUC flows afterward along the equator until the South American coast, where it takes different pathways. It turns northward and also to a lesser extent southward before it streams eventually along shore off the western coast of Colombia and Peru, respectively. The latter connection contributes to feed

the PCUC [Montes *et al.*, 2010]. The obstruction of the EUC flow by the Galapagos Islands creates an additional branch that diverts south-southeastward to join and reinforce the pSSCC, as previously suggested by Karinauskas *et al.* [2007]. This vein flows between 3°S and 5°S, parallel to the equator, until it reaches the Peruvian coast, where it joins the upper PCUC [Montes *et al.*, 2010].

### 3.4.2. Lagrangian Trajectories of Equatorial Subsurface Currents

[36] In order to classify the typical trajectories followed by particles within the three equatorial subsurface currents, numerical floats were released at 92°W (between 10°S and 2.5°N to span the location of all the currents) above 400 m depth during all days of the cold (October–December 1999) and warm (October–December 2002) phases of ENSO (see next subsection for details about the sampling strategy). Figure 8b shows a representative subset of these trajectories, with daily positions displayed throughout two years. It summarizes the generic pathways that we obtained without any distinction between the different ENSO phases.

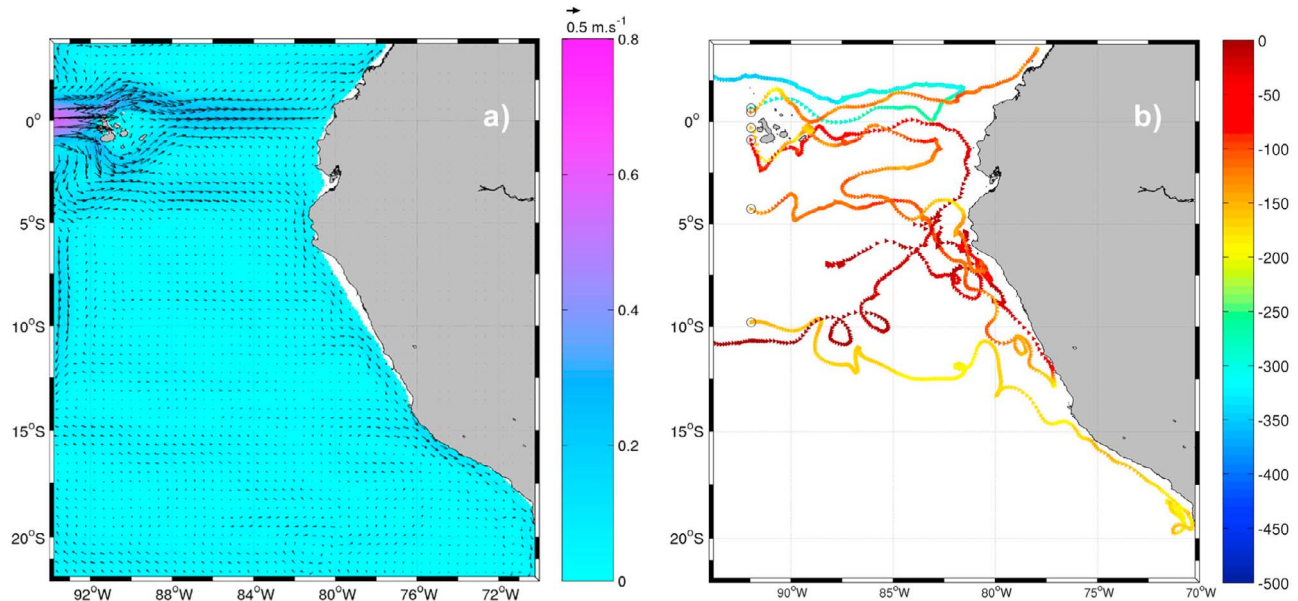


**Figure 8.** (a) Model velocity field at 100 m depth for mean conditions (with one vector every fifth grid point). Vectors are scaled according to the reference shown at the upper right-hand corner, and the color bar indicates speed in  $\text{m s}^{-1}$ . (b) Typical trajectories obtained for floats released in the equatorial subsurface currents at  $92^\circ\text{W}$  and integrated forward in time. Circles indicate the initial position of each float, and the along-trajectory depth is colored according to the color bar (with values in m).

[37] These pathways bring out the role of barrier played by the Galapagos Islands on the equatorial flow. The EUC is split around the islands into two eastward flowing branches, north and south of the equator. These branches recombine just east of the islands. Then the flow is eastward all the way to the region off Ecuador, where a bifurcation occurs. The floats that turn north into the Northern Hemisphere either flow along the coast to enter the Panama Bight at subsurface depths or come back west to become part of surface or subsurface westward flows on either side of the EUC. The floats that move southward after the bifurcation either upwell to the surface at the equator, close to the coast off Ecuador or northern Peru, and become part of westward or southwestward currents, or join the pSSCC to flow toward Peru before ultimately becoming part of the PCUC. The floats attached to the SSCCs move eastward or southwestward until they get near the coast, where some of them join the PCUC and flow poleward and where some others upwell and escape eventually the model domain at its western and southwestern edges within surface currents.

### 3.4.3. Transports of Equatorial Subsurface Currents During Cold and Warm Phases of ENSO

[38] To investigate the transports associated with each equatorial subsurface current, we selected for a Lagrangian analysis the geographic area from  $10^\circ\text{S}$  to  $2.5^\circ\text{N}$  and from  $92^\circ\text{W}$  to the west coast of South America, which encompasses the ECS of the eastern tropical Pacific. The northern and southern boundaries of the selected area are both subdivided into two distinct sections (see section 2.2 and Figures 1 and 8). We use the four resulting northwestern, northeastern, southwestern, and southeastern sections to intercept the trajectories originating in the western section (located at  $92^\circ\text{W}$ , across the ECS). The particles are initialized according to the strategy defined in section 2.2 during

the ENSO cold and warm phases, with the use of about 5,000,000 particles in each case. They are traced forward in time for a maximum duration of 1000 days until they reach a control section. The particles that recirculate back to  $92^\circ\text{W}$  are decomposed into three subsets according to their initial latitude on the western section. These subsets match conveniently the latitudinal ranges of the sSSCC ( $10^\circ\text{S}$ – $6^\circ\text{S}$ ), the pSSCC ( $6^\circ\text{S}$ – $2^\circ\text{S}$ ), and the EUC ( $2^\circ\text{S}$ – $2^\circ\text{N}$ ).

[39] Incoming and outgoing transports over the edges of our domain are summarized in Table 1 for particles initialized during both La Niña (October–December 1999) and El Niño (October–December 2002) periods. The transports inferred from our Lagrangian analysis are built on the individual weights of the numerical floats that keep a zonal Lagrangian velocity eastward for at least 30 days from  $92^\circ\text{W}$ . The particles that recirculate to  $92^\circ\text{W}$  in fewer than 30 days are excluded from the calculations since they only correspond to a fast seesaw movement around  $92^\circ\text{W}$ , which can hardly be associated with a genuine mass transfer. The average western inflow stemming from the equatorial subsurface current system during the cold phase is 27.3 Sv, out of which 14.9, 7.0, and 5.4 Sv originate in the EUC, pSSCC, and sSSCC, respectively. During the warm phase, the average inflow is reduced by  $\sim 27\%$  to 20 Sv, out of which 7.7, 4.9, and 7.4 Sv originate in the EUC, pSSCC, and sSSCC, respectively. The reduction of inflow during the warm phase is mainly caused by a weaker EUC transport but also, to a lesser extent, by a weaker pSSCC. The sSSCC transport, however, presents an increase of  $\sim 2$  Sv, which is consistent with the Eulerian view discussed in section 3.1. Indeed, during El Niño, tropical instability waves are substantially reduced, which in turn may weaken the strength of the EUC [Vecchi and Harrison, 2000; Yu and Liu, 2003; An, 2008, 2009]. The increase in sSSCC transport might be related to the more pronounced and also

**Table 1.** Incoming Western Subsurface Transport at 92°W During El Niño and La Niña Corresponding Outflows out of the Domain of the Lagrangian Study<sup>a</sup>

	Western Inflow Into the ETP		Western–92°W		Northwestern		Northeastern		Southwestern		Southeastern	
	Oct–Dec	Dec	Oct–Dec	Dec	Oct–Dec	Dec	Oct–Dec	Dec	Oct–Dec	Dec	Oct–Dec	Dec
<i>1999</i>												
Total	27.3	28.6	14.3	13.7	6.1	7.2	2.0	2.3	3.3	3.7	1.6	1.7
EUC	14.9	16.5	6.3	5.9	6.0	7.2	2.0	2.3	0.2	0.5	0.3	0.7
pSSCC	7.0	7.1	5.5	5.6	0.1	0.0	0.0	0.0	0.5	0.6	0.9	0.8
sSSCC	5.4	5.0	2.5	2.2	0.0	0.0	0.0	0.0	2.6	2.6	0.4	0.2
<i>2002</i>												
Total	20.0	12.7	12.1	9.3	1.6	1.1	0.7	0.1	5.0	1.9	0.7	0.2
EUC	7.7	4.4	5.1	3.1	1.6	1.1	0.7	0.1	0.3	0.1	0.1	0.0
pSSCC	4.9	2.4	3.5	1.7	0.0	0.0	0.0	0.0	1.1	0.5	0.3	0.1
sSSCC	7.4	5.9	3.5	4.5	0.0	0.0	0.0	0.0	3.6	1.3	0.3	0.1

<sup>a</sup>Transport is given in Sv. El Niño was during October–December 1999 and December 1999 and La Niña was during October–December 2002 and December 2002.

more southern position of the density front delimiting the southern edge of the pool of anomalous light equatorial waters during the developed phase of El Niño (see Figures 5c and 5f). This front has been shown to efficiently sustain a conduit of warm water from the equatorial region toward the Peruvian coast, as demonstrated for El Niño 1997–1998 [Colas *et al.*, 2008].

[40] During the cold phase of ENSO, 29.6% of the total western subsurface inflow leaves the study region at its northern boundary: 22.3% (6.1 Sv) and 7.3% (2 Sv) across the northwestern and northeastern sections, respectively. The proportion that connects to the southern boundary is only 18%: 12.1% (3.3 Sv) and 5.9% (1.6 Sv) across the southwestern and southeastern sections, respectively. In fact, more than half of the inflow (14.3 Sv) recirculates back to the release section before it can intercept either the southern or northern section. During the warm phase of ENSO, the fate of the western inflow is distributed differently. Only 11.5% of it reaches the northern boundary: 8% (1.6 Sv) and 3.5% (0.7 Sv) across the northwestern and northeastern sections, respectively. The proportion transmitted to the southern boundary is much larger (28.5%): 25% (5 Sv) and 3.5% (0.7 Sv) across the southwestern and southeastern sections, respectively. Again, a large fraction of the inflow connects back to the release section (more than 60%).

[41] The previous experiments are analyzed for the particles initialized only in December, the month during which the total western inflow is either maximum during the cold phase (1999) or minimum during the warm phase (2002). The incoming transport in December 1999 is only 1.4 Sv above its mean value over October–December 1999, but it is reduced drastically by 40% in December 2002 with respect to its average over October–December 2002. This result underscores the highly variable equatorial dynamics, here mostly related to weaker EUC and pSSCC transports (Table 1).

[42] Our results suggest that for both phases of ENSO most (>50%) of the incoming eastward subsurface flow at 92°W circulates in the eastern equatorial Pacific before being upwelled and sent back westward within the SEC or recirculates within adjacent westward flowing subsurface currents. This description is consistent with the results obtained by Montes *et al.* [2010], although their analysis was restricted to a climatological situation without ENSO-like variability.

[43] The export across the northern boundary originates fully from the EUC (see Table 1). It represents a significant portion of the EUC transport: 30% during El Niño, ~50% during La Niña. The difference between the two phases is mainly due to the eastward and deeper extension of the EUC during La Niña. This makes EUC particles less subject to equatorial upwelling and to surface westward export. The particles are thus more likely to reach the coastal region and to be advected northward (see Figure 8). Thus, since the EUC transport during La Niña is twice as large as during El Niño, the export to the northern boundary is much stronger in the cold phase.

[44] During El Niño, a large fraction of the ECS transport is exported across the southern boundary, especially the southwestern section. Indeed, this export is mainly supplied (by more than 90%) by waters from the SSCCs and the SSCCs represent a larger fraction of the ECS transport during El Niño than during La Niña conditions (61 and 45%, respectively).

#### 3.4.4. ECS-PCUC Connections: Lagrangian Stream Functions

[45] For climatological conditions and in a regional model with its western open boundary located at 92°W, Montes *et al.* [2010] described the pathways of numerical floats that were launched between 86°W and 87°W within each equatorial subsurface current and that contributed to the PCUC. Their Lagrangian description was obtained from the analysis of two numerical simulations that were identical in most aspects, but that used different data (SODA and OCCAM) to constrain the open boundaries. Their results showed that the EUC followed equally a direct and an indirect route to reach the PCUC. The direct route was identified as a quasi-zonal flow along the equator. The indirect route was identified as an eastward flow along the equator over several degrees of longitude before meandering to the southwest until merging with the eastward pSSCC and eventually reaching the coastal region. On the contrary, one route only was obtained for both SSCCs. We adjust here our Lagrangian analysis in order to assess how these pathways and their respective contributions to the PCUC are altered during the cold and warm phases of ENSO. Therefore, we focus only on the particles that do make the connection between the ECS at 92°W (with initial positions above 400 m and for the three months representative of

La Niña and El Niño) and the southeastern section at 10°S that encompasses the PCUC. The trajectories of these particles are used to compute the horizontal Lagrangian stream function  $\psi_h$  related to the vertically integrated transport of the flow [Blanke *et al.*, 1999] transmitted from 92°W to 10°S. Figure 9 shows our results separately for each equatorial subsurface current, both for La Niña (October–December 1999) and El Niño (October–December 2002) conditions. Together with the contours of  $\psi_h$ , the position statistics related to the particles that flow eventually within the PCUC at 10°S allow the detailed study of the pathways followed by the ECS waters.

[46] During La Niña, the stream function produces three well-separated zonal (at least from 92°W to 84°W) bands of enhanced transport contributing to the PCUC. At 92°W their latitudinal distribution corresponds to the equatorial subsurface currents identified and described in our Eulerian analysis (Figure 5b). The statistics about the initial depth of the particles also match their depth ranges (40–350 m). The contribution from the EUC (0.3 Sv) stems mainly from the branch that skirts the Galapagos Islands to the north and from depths that correspond to the EUC core. In the same way as under climatological mean conditions [Montes *et al.*, 2010], the released particles follow either the direct or the indirect route introduced previously. The former is, however, clearly favored during the cold phase of ENSO, unlike during climatological mean conditions. A similar behavior is found for the pSSCC. A portion of the pSSCC (0.9 Sv), which eventually feeds the PCUC, follows a direct route that is made up of a zonal pathway until the coast of Peru (at ~4.5°S). The particles that define the other portion of the pSSCC follow an indirect route. They flow zonally for several degrees of longitude then turn southwestward until they join the sSSCC and further flow toward the Peruvian coast. Then they continue poleward within the PCUC, west of the EUC-originating water. The water from the sSSCC (0.4 Sv) that feeds the PCUC follows only one pathway. It is a quasi-zonal flow toward the coast turning southward into an alongshore flow, which shapes the westernmost portion of the PCUC.

[47] During El Niño, the pattern of the stream function for the connection from 92°W to the PCUC is much less marked zonally than during La Niña, and the intensity of the transfer amounts only to 0.7 Sv. Nevertheless, quasi-zonal displacements still prevail before approaching the South American continent. The shallow (50–100 m) core of the EUC that skirts the Galapagos Archipelago to the south is limited to 0.1 Sv, with the northern branch being apparently absent. Its pathway is heterogeneous in the sense that the streamlines occupy meridional positions between 0°S and 4°S, which reflects some partial merging with the pSSCC as already discussed in the Eulerian analysis (Figure 5f). The contribution of the pSSCC (estimated between 2°S and 6°S) is also reduced during the warm event, down to 0.3 Sv. It flows southeastward until it reaches ~7°S. Then it flows parallel to the coast approximately within the central portion of the PCUC. The waters of the sSSCC are also flowing south-

eastward until close to 9°S and then turn southward as during La Niña conditions; the transport transmitted (0.3 Sv) is quite similar to the cold-phase transport. During El Niño conditions, only one pathway toward the PCUC is identified for each equatorial subsurface current and the initial positions of all the particles are located at a shallower depth at 92°W, between 10 and 300 m, which is most likely related to the outcrop of the sSSCC and to the limited vertical extension of the equatorial currents at that time (Figure 5c). The northwest-southeast orientation of the pathways found for all equatorial subsurface currents during El Niño is consistent with the similar orientation of the density front diagnosed by Colas *et al.* [2008] between lighter equatorial and heavier subtropical subsurface waters in the ETP for the 1997–1998 El Niño peak.

[48] Our results indicate that the total transport of waters achieved by equatorial subsurface currents toward the PCUC is reduced by more than half during the warm phase of ENSO and corresponds mostly to a reduction in the transport of the EUC and pSSCC. During the cold phase, interestingly, both EUC pathways as well as those of the SSCCs subsist, just as under climatological mean conditions. This result, obtained here for the Lagrangian analysis of a regional ocean model of the ETP, is in agreement with the premise that La Niña is an amplification of the mean conditions in the eastern Pacific, as suggested for instance by Pezzulli *et al.* [2005] and Guilyardi [2007].

[49] The water mass transfer from 92°W to the coast of South America at 10°S is here described in terms of individual trajectories for which a histogram of the age distribution, weighted by the individual weights, can be calculated (not shown). The transfer time of particles to 10°S spans several years (up to 1000 days), and the median values are 476 days and 424 days for the transfers initiated in October–December 1999 and October–December 2002, respectively. The particles mainly reach 10°S in austral winter months during the two years following their release, under both warm and cold conditions, though a faster connection (which will be further discussed below) also occurs in 60–100 days during the El Niño phase.

[50] The age statistics can also be differentiated according to the followed vein of current. Median times increase with latitude, with the sSSCC connection (~390 days) and the EUC connection (~560 days) being the fastest and slowest ones, respectively. Therefore, the waters that leave 92°W in October–December 1999 and 2002 arrive on average more than one year later at 10°S, within a current system that may differ from the structures presented in Figure 6.

[51] To investigate this issue and add vertical dimension to the circulation patterns shown in Figure 9, we remap at 10°S the individual weights carried by the particles that participate in the connection made with the southeastern section. For this remapping, the underlying mesh has a uniform 0.1° zonal and 20 m vertical resolution. We normalize the sum of the individual weights of the particles that reach each cell by the

**Figure 9.** Horizontal stream functions  $\psi_h$  related to the vertically (0–400 m) integrated transport of the flow from 92°W to the southeastern section (at 10°S, from 82°W to the coastline) during La Niña (October–December 1999; Figures 9a, 9c, and 9e) and El Niño (October–December 2002; Figures 9b, 9d, and 9f) computed for each subsurface current: (a, b) EUC, (c, d) pSSCC, and (e, f) sSSCC. The value of  $\psi_h$  is arbitrarily set to 0 over South America. The contour interval is 0.01 Sv. The colors and the labels of the streamlines indicate values of the transport stream function.

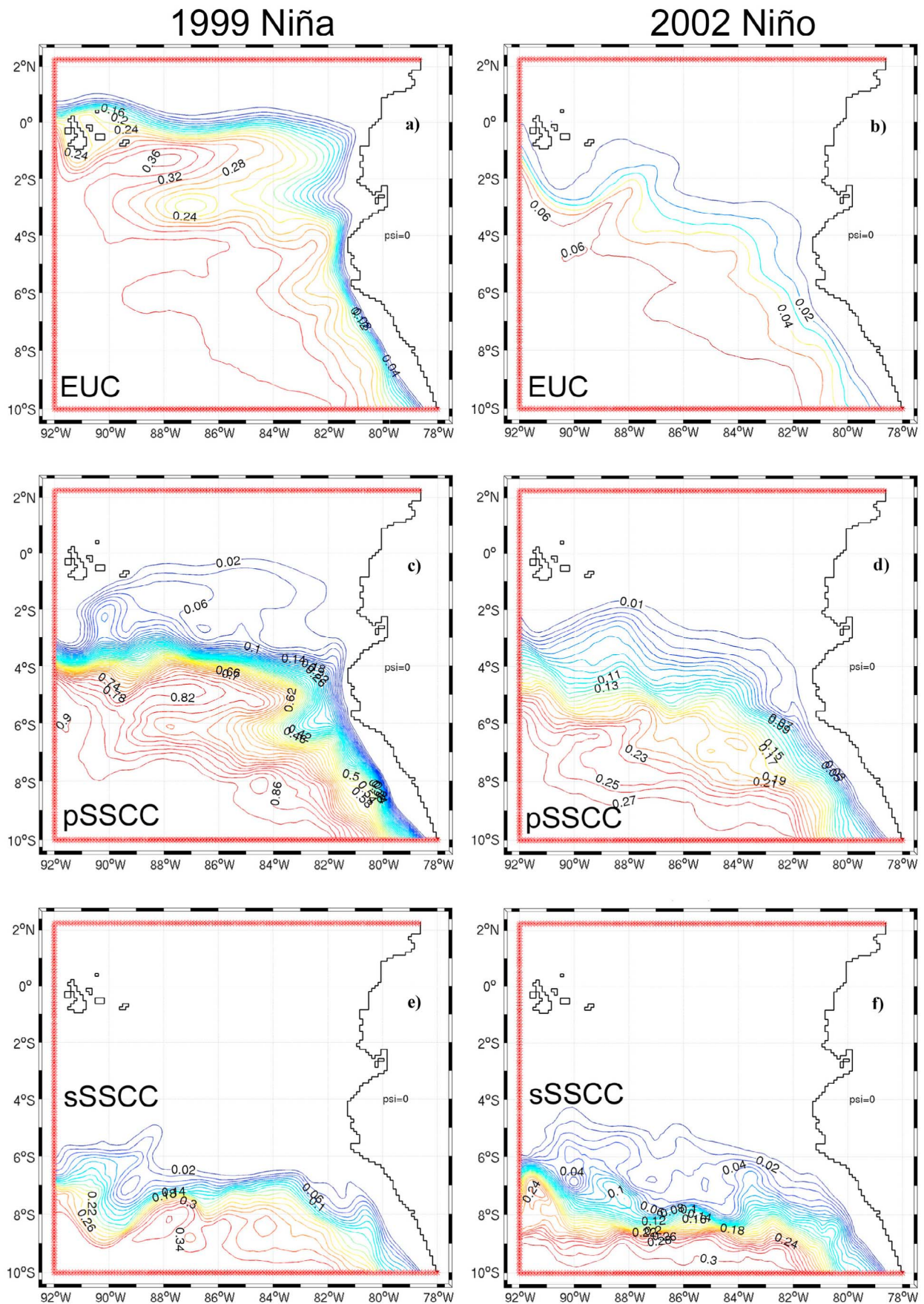
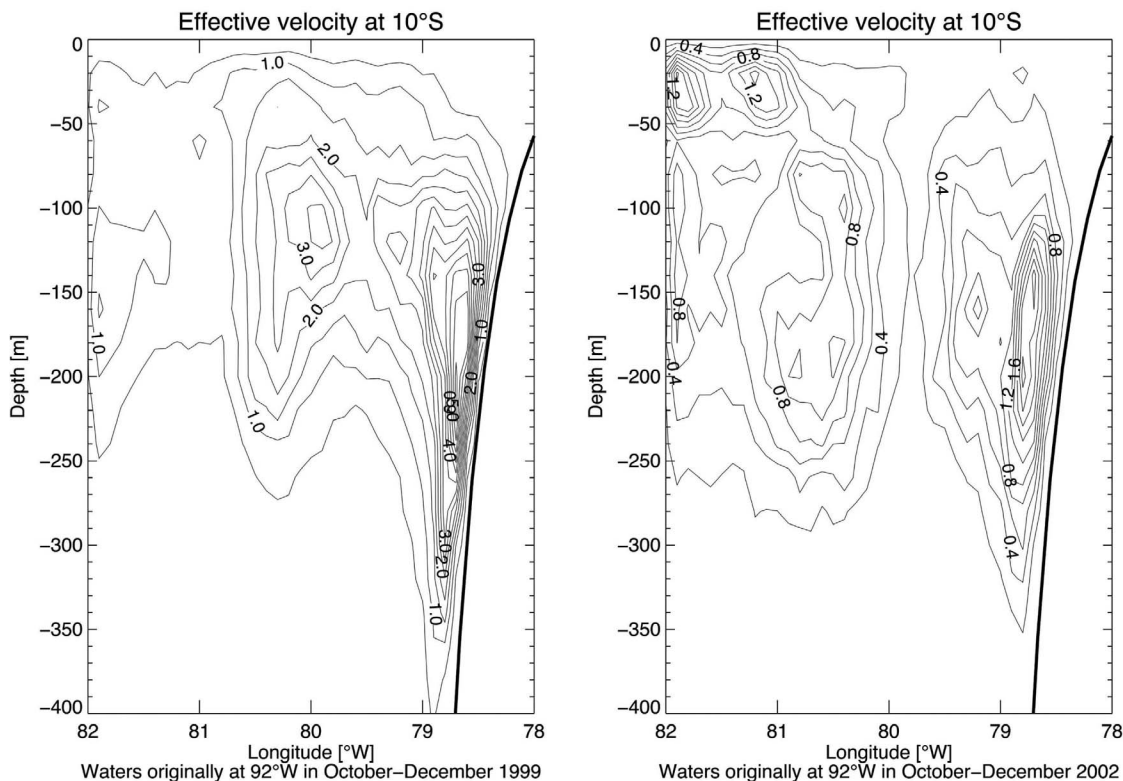


Figure 9



**Figure 10.** Average velocity cross section at  $10^{\circ}\text{S}$  associated with the poleward export of equatorial waters from the EUC, pSSCC, and sSSCC initially considered at  $92^{\circ}\text{W}$  during (left) October–December 1999 and (right) October–December 2002. The contour interval is  $0.5\text{ cm s}^{-1}$  and  $0.2\text{ cm s}^{-1}$  for the cold and warm phase, respectively. See text for details about the calculation of this effective velocity.

surface area of the cell. The resultant effective velocity is southward by construction and is expressed in  $\text{m s}^{-1}$  (Figure 10). It can be readily compared with the mean Eulerian velocity profiles shown in Figure 6. The difference in magnitude is explained by the fact that only a fraction of the southward flow within the PCS is connected straight to the ECS considered at  $92^{\circ}\text{W}$ . The geometry of the velocity cores provides, however, useful information about the main dynamical veins actually followed by the equatorial waters transferred to  $10^{\circ}\text{S}$  and their capture by the PCS (see Figure 6). For both ensembles of particles, initialized in October–December 1999 and 2002, the outflow at  $10^{\circ}\text{S}$  is made mostly of two cores. One core is rather compact and flows next to the continental shelf at 150–200 m depth. The second core is 200–250 km offshore and is centered at a slightly shallower depth (around 120 m). The latter reminds one of the structures found at  $10^{\circ}\text{S}$  during La Niña for the poleward currents (Figure 6b), and much less of the El Niño situation for which poleward currents flow closer to the surface with much less vertical extent (Figure 6a).

[52] Note that a clear offshore near-surface core is obtained during El Niño conditions, around  $81^{\circ}\text{W}$ – $82^{\circ}\text{W}$  and at depth 20–60 m. This core is also present on the vertical Eulerian velocity section (Figure 6c), again for El Niño conditions only. The analysis of the ages associated with this core shows that this pathway corresponds to the fast connection of 60–100 days diagnosed during El Niño. The trajectories of these particles (not shown) roughly coincide with the position of

the sea level front delimiting the El Niño warm anomaly (Figure 2c). This confirms that this front sustains an advection of warm water from the equatorial region toward the Peruvian coast, as shown by *Colas et al.* [2008] for the 1997–1998 El Niño.

[53] Results based on Lagrangian times of arrival show that the calendar months conducive at  $10^{\circ}\text{S}$  to the southern export of equatorial waters are June–July and August–September, for La Niña 1999–2001 and El Niño 2002–2003, respectively. This suggests that ambient conditions along the Peruvian coast also modulate the poleward export of equatorial waters: Winter velocity conditions seem to be more favorable to channel the water originating at  $92^{\circ}\text{W}$  out of the equatorial domain.

#### 4. Conclusion

[54] In this study, we presented an interannual solution for the ocean circulation in the ETP encompassing the 1999–2005 period that covers in particular a strong La Niña (1999–2000) and a moderate El Niño (2002–2003). Our results are based on a high-resolution numerical model, ROMS, forced by 1999–2005 QuikSCAT winds at its surface and SODA-POP model data at its open boundaries. The assessment of the model skill showed that our simulation reproduces fairly well-known features of the ETP dynamics during mean conditions, as well as during the cold and warm ENSO events. Our model especially accounts for the reemerging and

weakening of the EUC branches after skirting round the Galapagos Islands. The vertical structure of the three subsurface equatorial currents (EUC, pSSCC, and sSSCC) changes a lot when switching from normal conditions to a La Niña or El Niño state. During the cold phase of ENSO, the three currents are well developed, are associated with denser waters, and have a vertical extent deeper than normal, with a total transport of 31 Sv. On the other hand, during the warm phase, they flow at shallower depths, they are associated with lighter waters, and they transport only a total of 16 Sv. Similarly, the PCUC shows contrasted behaviors according to the surrounding climate conditions. During the cold phase of ENSO, it is associated with denser waters and has a vertical extent deeper than normal, with a total transport of 1.6 Sv. During the warm phase, it flows at a shallower depth and it is associated with lighter waters, but with a larger transport (3.0 Sv). More than half of the incoming transport of the equatorial subsurface currents recirculates westward with the SEC and companion subsurface flows during both ENSO phases. The remaining incoming transport goes to the extra-equatorial region: 30% (11%) of the ECS transport at 92°W crosses the section at 2.5°N and 17% (28%) goes southward through the section at 10°S, during the cold (warm) phase of ENSO. The equatorial subsurface currents, and especially the pSSCC, contribute to 80% of the PCUC transport during the cold phase. This ratio falls down to only 20% during the warm phase of ENSO.

[55] These results are obtained for only one cold and one warm period over the years 1999–2003. Composite ENSO patterns of the ECS and PCS for the period 1980–2000 present many similarities with those of the 1999–2003 period, though obviously the generalization of these results to any ENSO event should be considered with caution.

[56] **Acknowledgments.** We thank the Deutscher Akademischer Austausch Dienst (DAAD) and POGO-SCOR for providing the funding to visit the Institut für Meereskunde (IFM-GEOMAR) and the Laboratoire de Physique des Océans (LPO), respectively. We thank Nicolas Grima for his help and precious advice on ARIANE. We also thank IMARPE for providing us with sea surface temperature time series of six coastal stations. The altimeter products were produced by SSALTO-DUACS and distributed by AVISO with support from CNES. The AVHRR-Pathfinder SST data were obtained from the Physical Oceanography Distributed Active Archive Center (PO.DAAC) at the NASA Jet Propulsion Laboratory. Ivonne Montes was funded by the DAAD scholarship program and by the Chilean National Research Council (project 15010007) through the FONDAP-COPAS Center. Francois Colas was partly funded by the ANR-VMCS-2008 Peru Ecosystem Projection Scenarios (PEPS) project.

## References

- An, S.-I. (2008), Interannual variations of the tropical ocean instability wave and ENSO, *J. Clim.*, *21*, 3680–3686, doi:10.1175/2008JCLI1701.1.
- An, S.-I. (2009), A review of interdecadal changes in the nonlinearity of the El Niño–Southern Oscillation, *Theor. Appl. Climatol.*, *97*, 29–40, doi:10.1007/s00704-008-0071-z.
- Barnier, B., L. Siefridt, and P. Marchesiello (1995), Thermal forcing for a global ocean circulation model using a three-year climatology of ECMWF analyses, *J. Mar. Syst.*, *6*, 363–380, doi:10.1016/0924-7963(94)00034-9.
- Blanco, J. L., M.-E. Carr, A. Thomas, and P. T. Strub (2002), Hydrographic conditions off of northern Chile during the 1996–1998 La Niña and El Niño, *J. Geophys. Res.*, *107*(C3), 3017, doi:10.1029/2001JC001002.
- Blanke, B., and S. Raynaud (1997), Kinematics of the Pacific Equatorial Undercurrent: An Eulerian and Lagrangian approach from GCM results, *J. Phys. Oceanogr.*, *27*, 1038–1053, doi:10.1175/1520-0485(1997)027<1038:KOTPEU>2.0.CO;2.
- Blanke, B., M. Arhan, G. Madec, and S. Roche (1999), Warm water paths in the equatorial Atlantic as diagnosed with a general circulation model, *J. Phys. Oceanogr.*, *29*, 2753–2768, doi:10.1175/1520-0485(1999)029<2753:WWPITE>2.0.CO;2.
- Brainard, R. E., and D. R. McLain (1987), Seasonal and interannual subsurface temperature variability off Peru, 1952–1984, in *The Peruvian Anchoveta and Its Upwelling Ecosystem: Three Decades of Change*, *ICLARM Stud. Rev. Ser.*, vol. 15, edited by D. Pauly and I. Tsukayama, pp. 14–45, Inst. del Mar del Perú, Callao, Peru.
- Brink, K. H. (1982), A comparison of long coastal trapped wave theory with observations off Peru, *J. Phys. Oceanogr.*, *12*, 897–913, doi:10.1175/1520-0485(1982)012<0897:ACOLCT>2.0.CO;2.
- Capet, X. J., P. Marchesiello, and J. C. McWilliams (2004), Upwelling response to coastal wind profiles, *Geophys. Res. Lett.*, *31*, L13311, doi:10.1029/2004GL020123.
- Carton, J. A., and B. S. Giese (2008), A reanalysis of ocean climate using Simple Ocean Data Assimilation (SODA), *Mon. Weather Rev.*, *136*, 2999–3017, doi:10.1175/2007MWR1978.1.
- Colas, F., X. Capet, J. C. McWilliams, and A. Shchepkin (2008), 1997–1998 El Niño off Peru: A numerical study, *Prog. Oceanogr.*, *79*, 138–155, doi:10.1016/j.pocan.2008.10.015.
- Colas, F., J. C. McWilliams, X. Capet, and J. Kurian (2011), Heat balance and eddies in the Peru–Chile current system, *Clim. Dyn.*, doi:10.1007/s00382-011-1170-6, in press.
- Croquette, M., G. Eldin, C. Grados, and M. Tamayo (2007), On differences in satellite wind products and their effects in estimating coastal upwelling processes in the south-east Pacific, *Geophys. Res. Lett.*, *34*, L11608, doi:10.1029/2006GL027538.
- da Silva, A. M., C. C. Young-Molling, and S. Levitus (Eds.) (1994), *Atlas of Surface Marine Data 1994*, vol. 1, *Algorithms and Procedures*, NOAA Atlas NESDIS, vol. 6, 83 pp., NOAA, Silver, Spring, Md.
- Donohue, K. A., E. Firing, G. D. Rowe, A. Ishida, and H. Mitsudera (2002), Equatorial Pacific subsurface countercurrents: A model-data comparison in stream coordinates, *J. Phys. Oceanogr.*, *32*, 1252–1264, doi:10.1175/1520-0485(2002)032<1252:EPSCAM>2.0.CO;2.
- Ducet, N., P. Le Traon, and G. Reverdin (2000), Global high-resolution mapping of ocean circulation from TOPEX/POSEIDON and ERS-1 and -2, *J. Geophys. Res.*, *105*, 19,477–19,498, doi:10.1029/2000JC900063.
- Echevin, V., F. Colas, A. Chaigneau, and P. Penven (2011), Sensitivity of the Northern Humboldt Current System nearshore modeled circulation to initial and boundary conditions, *J. Geophys. Res.*, *116*, C07002, doi:10.1029/2010JC006684.
- Enfield, D. B., and J. S. Allen (1980), On the structure and dynamics of monthly mean sea level anomalies along the Pacific coast of North and South America, *J. Phys. Oceanogr.*, *10*, 557–578, doi:10.1175/1520-0485(1980)10<0557:OTSADO>2.0.CO;2.
- Fiedler, P. C., F. P. Chavez, D. W. Behringer, and S. B. Reilly (1992), Physical and biological effects of Los Niños in the eastern tropical Pacific, 1986–1989, *Deep Sea Res.*, *39*(2), 199–219, doi:10.1016/0198-0149(92)90105-3.
- Guilyardi, E. (2007), *Understanding El Niño in State-of-the-Art Climate Models: New Perspectives*, Habilitation à Diriger des Rech., Paris.
- Huyer, A., R. L. Smith, and T. Paluszkiwicz (1987), Coastal upwelling off Peru during normal and El Niño times, *J. Geophys. Res.*, *92*, 14,297–14,307, doi:10.1029/JC092iC13p14297.
- Huyer, A., M. Knoll, T. Paluszkiwicz, and R. L. Smith (1991), The Peru Undercurrent: A study of variability, *Deep Sea Res.*, *38*, S247–S271.
- Izumo, T. (2005), The equatorial undercurrent, meridional overturning circulation, and their roles in mass and heat exchanges during El Niño events in the tropical Pacific Ocean, *Ocean Dyn.*, *55*, 110–123, doi:10.1007/s10236-005-0115-1.
- Izumo, T., J. Picaut, and B. Blanke (2002), Tropical pathways, equatorial undercurrent variability and the 1998 La Niña, *Geophys. Res. Lett.*, *29*(22), 2080, doi:10.1029/2002GL015073.
- Johnson, G. C., and D. W. Moore (1997), The Pacific Subsurface Countercurrents and an inertial model, *J. Phys. Oceanogr.*, *27*, 2448–2459, doi:10.1175/1520-0485(1997)027<2448:TPSCAA>2.0.CO;2.
- Johnson, G. C., B. M. Sloyan, W. S. Kessler, and K. E. McTaggart (2002), Direct measurements of upper ocean currents and water properties across the tropical Pacific during the 1990s, *Prog. Oceanogr.*, *52*, 31–61, doi:10.1016/S0079-6611(02)00021-6.
- Karnauskas, K. B., R. Murtugudde, and A. J. Busalacchi (2007), The effect of the Galapagos Islands on the equatorial Pacific cold tongue, *J. Phys. Oceanogr.*, *37*, 1266–1281, doi:10.1175/JPO3048.1.
- Kessler, W. S. (2006), The circulation of the eastern tropical Pacific: A review, *Prog. Oceanogr.*, *69*, 181–217, doi:10.1016/j.pocan.2006.03.009.
- Kessler, W. S., and M. J. McPhaden (1995), The 1991–93 El Niño in the central Pacific, *Deep Sea Res. Part II*, *42*, 295–333, doi:10.1016/0967-0645(95)00041-N.

- Latif, M., and N. Keenlyside (2009), El Niño/Southern Oscillation response to global warming, *Proc. Natl. Acad. Sci. U. S. A.*, *106*(49), 20,578–20,583, doi:10.1073/pnas.0710860105.
- Liu, W. T., W. Tang, and P. S. Polito (1998), NASA scatterometer provides global ocean-surface wind fields with more structures than numerical weather prediction, *Geophys. Res. Lett.*, *25*, 761–764, doi:10.1029/98GL00544.
- Lukas, R. (1986), The termination of the Equatorial Undercurrent in the eastern Pacific, *Prog. Oceanogr.*, *16*, 63–90, doi:10.1016/0079-6611(86)90007-8.
- McCreary, J. P., Jr., P. Lu, and Z. Yu (2002), Dynamics of the Pacific Subsurface Countercurrents, *J. Phys. Oceanogr.*, *32*(8), 2379–2404, doi:10.1175/1520-0485(2002)032<2379:DOTPSC>2.0.CO;2.
- McPhaden, M. J. (1984), On the dynamics of equatorial subsurface counter currents, *J. Phys. Oceanogr.*, *14*, 1216–1225, doi:10.1175/1520-0485(1984)014<1216:OTDOES>2.0.CO;2.
- McPhaden, M. J. (2004), Evolution of the 2002–03 El Niño, *Bull. Am. Meteorol. Soc.*, *85*, 677–695, doi:10.1175/BAMS-85-5-677.
- McPhaden, M. J., and S. P. Hayes (1990), Variability in the eastern equatorial Pacific during 1986–1988, *J. Geophys. Res.*, *95*, 13,195–13,208, doi:10.1029/JC095iC08p13195.
- McPhaden, M. J., S. E. Zebiak, and M. H. Glantz (2006), ENSO as an integrating concept in earth science, *Science*, *314*, 1740–1745, doi:10.1126/science.1132588.
- Montes, I., F. Colas, X. Capet, and W. Schneider (2010), On the pathways of the equatorial subsurface currents in the eastern equatorial Pacific and their contributions to the Peru–Chile Undercurrent, *J. Geophys. Res.*, *115*, C09003, doi:10.1029/2009JC005710.
- Penven, P., V. Echevin, J. Pasapera, F. Colas, and J. Tam (2005), Average circulation, seasonal cycle, and mesoscale dynamics of the Peru Current System: A modeling approach, *J. Geophys. Res.*, *110*, C10021, doi:10.1029/2005JC002945.
- Penven, P., P. Marchesiello, L. Debreu, and J. Lefevre (2008), Software tools for pre- and post-processing of oceanic regional simulations, *Environ. Modell. Software*, *23*, 660–662, doi:10.1016/j.envsoft.2007.07.004.
- Pezzulli, S., D. B. Stephenson, and A. Hannachi (2005), The variability of seasonality, *J. Clim.*, *18*, 71–88, doi:10.1175/JCLI-3256.1.
- Pizarro, O., G. Shaffer, B. Dewitte, and M. Ramos (2002), Dynamics of seasonal and interannual variability of the Peru–Chile Undercurrent, *Geophys. Res. Lett.*, *29*(12), 1581, doi:10.1029/2002GL014790.
- Rowe, G. D., E. Firing, and G. C. Johnson (2000), Pacific Equatorial Subsurface Countercurrent velocity, transport, and potential vorticity, *J. Phys. Oceanogr.*, *30*, 1172–1187, doi:10.1175/1520-0485(2000)030<1172:PESCVT>2.0.CO;2.
- Shaffer, G., O. Pizarro, L. Djurfeldt, S. Salinas, and J. Rutllant (1997), Circulation and low frequency variability near the Chile coast: Remotely forced fluctuations during the 1991–1992 El Niño, *J. Phys. Oceanogr.*, *27*, 217–235, doi:10.1175/1520-0485(1997)027<0217:CALFVN>2.0.CO;2.
- Shchepetkin, A. F., and J. C. McWilliams (2005), The regional oceanic modeling system (ROMS): A split-explicit, free-surface, topography following-coordinate oceanic model, *Ocean Modell.*, *9*, 347–404, doi:10.1016/j.ocemod.2004.08.002.
- Shchepetkin, A. F., and J. C. McWilliams (2009), Correction and commentary for “Ocean forecasting in terrain-following coordinates: Formulation and skill assessment of the regional ocean modeling system” by Haidvogel et al., *J. Comput. Phys.*, *228*, 8985–9000, doi:10.1016/j.jcp.2009.09.002.
- Smith, R. (1983), Peru coastal currents during El Niño: 1976 and 1982, *Science*, *221*, 1397–1399, doi:10.1126/science.221.4618.1397.
- Smith, W. H. F., and D. T. Sandwell (1997), Global seafloor topography from satellite altimetry and ship depth soundings, *Science*, *277*, 1956–1962, doi:10.1126/science.277.5334.1956.
- Steger, J. M., C. A. Collins, and P. C. Chu (1998), Circulation in the Archipelago de Colon (Galápagos Islands), *Deep Sea Res. Part II*, *45*, 1093–1114, doi:10.1016/S0967-0645(98)00015-0.
- Strub, P. T., J. M. Mesias, V. Montecino, J. Rutllant, and S. Salinas (1998), Coastal ocean circulation off western South America, in *The Sea*, vol. 11, edited by A. R. Robinson and K. H. Brink, pp. 273–314, John Wiley, Hoboken, N. J.
- Vecchi, G. A., and D. E. Harrison (2000), Tropical Pacific sea surface temperature anomalies, El Niño and equatorial westerly wind events, *J. Clim.*, *13*, 1814–1830, doi:10.1175/1520-0442(2000)013<1814:TPSSTA>2.0.CO;2.
- Wang, C., and P. C. Fiedler (2006), ENSO variability and the eastern tropical Pacific: A review, *Prog. Oceanogr.*, *69*, 239–266, doi:10.1016/j.pocan.2006.03.004.
- Wang, C., and J. Picaut (2004), Understanding ENSO physics—A review, in *Earth’s Climate: The Ocean–atmosphere Interaction*, *Geophys. Monogr. Ser.*, vol. 147, edited by C. Wang, S. -P. Xie, and J. A. Carton, pp. 21–48, AGU, Washington, D. C.
- Webb, D. J., A. C. Coward, B. A. de Cuevas, and C. S. Gwillam (1997), A multiprocessor Ocean General Circulation Model using message passing, *J. Atmos. Oceanic Technol.*, *14*, 175–183, doi:10.1175/1520-0426(1997)014<0175:AMOGCM>2.0.CO;2.
- Yu, J. -Y., and W. T. Liu (2003), A linear relationship between ENSO intensity and tropical instability wave activity in the eastern Pacific Ocean, *Geophys. Res. Lett.*, *30*(14), 1735, doi:10.1029/2003GL017176.
- B. Blanke, Laboratoire de Physique des Océans, UMR 6523, CNRS/Ifremer/IRD/UBO, 6 ave. Le Gorgeu, CS 93837, Brest F-29238, France.
- F. Colas, Institute of Geophysics and Planetary Physics, University of California, 405 Charles E. Young Dr., Los Angeles, CA 90095-1567, USA.
- V. Echevin, Laboratoire d’Océanographie et du Climat Expérimentation et Approches Numériques, IRD/IPSL/UPMC, 4 pl. Jussieu, Paris F-75252, France.
- I. Montes, Programa de Postgrado en Oceanografía, Departamento de Oceanografía, Universidad de Concepción, Barrio Universitario S/N, Cabina 5, Casilla 160-C Concepción, Chile. (ivonem@udec.cl)
- W. Schneider, Departamento de Oceanografía, Universidad de Concepción, Barrio Universitario S/N, Cabina 5, Casilla 160-C, Concepción, Chile.